

Stochastic resonance in vibrational polariton chemistry

Yaling Ke¹

Department of Chemistry and Applied Biosciences, ETH Zürich, 8093 Zürich, Switzerland

(*Electronic mail: yaling.ke@phys.chem.ethz.ch)

In this work, we systematically investigate the impact of ambient noise intensity on the rate modifications of ground-state chemical reactions in an optical cavity under vibrational strong-coupling conditions. To achieve this, we utilize a numerically exact open quantum system approach—the hierarchical equations of motion in twin space, combined with a flexible tree tensor network state solver. Our findings reveal a stochastic resonance phenomenon in cavity-modified chemical reactivities: an optimal reaction rate enhancement occurs at an intermediate noise level. In other words, this enhancement diminishes if ambient noise, sensed by the cavity-molecule system through cavity leakage, is either too weak or excessively strong. In the collective coupling regime, when the cavity is weakly damped, rate enhancement strengthens as more molecules couple to the cavity. In contrast, under strong cavity damping, reaction rates decline as the number of molecules grows.

I. INTRODUCTION

Placing reactive molecules within an optical microcavity under conditions of vibrational strong coupling (VSC) has recently shown promise for manipulating chemical reactions, such as cavity catalysis and cavity-induced reaction selectivities, even in the absence of light.¹ This concept has been demonstrated in several experiments, which suggests that adjusting the distance between two reflective dielectric mirrors in a Fabry-Pérot cavity so that the cavity frequency resonates with specific molecular vibrations can alter reaction rates or product ratios.^{2–13} However, two independent experimental attempts to replicate these findings, while successfully reproducing VSC conditions, did not observe noticeable rate changes in an on-resonant cavity.^{14,15} Different outcomes in the experiments suggest that additional factors beyond VSC, factors that may have been previously overlooked, could play a critical role in achieving cavity-induced modifications of ground-state chemical reactivities. In this study, we aim to explore one such experimental variable: the damping strength of the cavity mode. This damping, caused by ambient noise surrounding the cavity due to the unavoidable cavity leakage, may influence the extent of cavity-induced rate modifications.

Naturally, this intriguing yet controversial phenomenon has spurred a substantial amount of theoretical research.^{16–33} Recent studies using quantum dynamical simulations underscore the necessity of a quantum discrete state description for both molecular vibrations and the cavity mode.^{1,2,34–37} However, this requirement introduces significant challenges, particularly in the collective regime, where a large ensemble of molecules couples to the cavity mode. To address the computational challenges, we employ the hierarchical equations (HEOM) of motion along with a tree tensor network state (TTNS) solver.⁴⁰ The HEOM method is a well-established, numerically exact approach for open quantum system dynamics,^{41–51} enabling a non-perturbative and non-Markovian treatment of system dynamics and bath-related observables. The TTNS,^{52–65} in addition, provides an efficient data compression scheme for storing and propagating the high-dimensional composite system-plus-bath wavefunction.

To gain a preliminary understanding of how chemical reactions inside a cavity respond to ambient noise—stemming from

interactions between the confined cavity mode and the continuum of far-field electromagnetic modes, which dampens the cavity’s oscillatory dynamics—we begin our study on the single-molecule level. Our results show that reaction rate enhancements within the cavity exhibit a typical stochastic resonance feature⁶⁶: neither excessively weak nor overly strong damping of cavity dynamics supports effective cavity-induced rate modifications. Instead, the rate constant inside a resonant cavity reaches its peak at an intermediate level of cavity damping. In the collective coupling regime, where multiple molecules are interconnected through a shared coupling with the cavity mode, rate modifications can display distinct behaviors as the system size grows. Under weak ambient noise, the rate enhancement strengthens as more molecules are coupled to the cavity mode. On the contrary, under conditions of strong cavity damping, the rate enhancement is attenuated with the increased number of coupled molecules. These observations lead us to ask an essential question: Could an ensemble of molecules on the macroscopic scale, immersed in a solvent and thus exposed to significant background noise, act cooperatively through collective coupling to the cavity mode, and synergetically harness a feeble fluctuation to optimize the reaction efficiency?

The following sections present a detailed account of our findings. Sec. II outlines an open quantum system model that describes chemical reactions in a condensed-phase optical cavity and the quantum dynamics methodology used. Sec. III presents and discusses the numerical results, followed by a summary and perspectives for our future research in Sec. IV.

II. THEORY

We consider an open quantum system model to study chemical reactions inside an optical cavity,

$$H = H_S + H_E, \quad (1)$$

where H_S describes the cavity-molecule system and H_E represents its surrounding environment.

The reaction dynamics of N_{mol} molecules coupled to a single-mode cavity is described by the Pauli-Fierz light-matter Hamiltonian in the dipole gauge under the long-wavelength

approximation^{34,67–69}

$$H_S = \overbrace{\frac{p_c^2}{2} + \frac{1}{2}\omega_c^2 \left(x_c + \sqrt{\frac{2}{\omega_c}} \eta_c \sum_{i=1}^{N_{\text{mol}}} \vec{\mu}_i(x_i) \cdot \vec{e} \right)^2}_{H_c(\mathbf{x})}} + \underbrace{\sum_{i=1}^{N_{\text{mol}}} \left[\frac{p_i^2}{2} + \frac{E_b}{a^4} (x_i - a)^2 (x_i + a)^2 \right]}_{H_{\text{mol}}^i} \quad (2)$$

The cavity mode is modeled as a harmonic oscillator with momentum p_c , coordinate q_c , and frequency ω_c . For convenience, we set $\hbar = 1$ throughout this work. The light-matter coupling strength is characterized by the parameter $\eta_c = \frac{1}{\omega_c} \sqrt{\frac{\omega_c}{2\epsilon_0 V}}$, where ϵ_0 is the permittivity of the medium within the cavity and V is the quantization volume of the electromagnetic mode. The unit vector \vec{e} points to the light polarization direction. Each molecule is represented by a reactive vibrational mode with mass-scaled momentum p_i , coordinate x_i , and a symmetric double-well potential energy surface with a barrier height E_b between two local minima at $x_i = \pm a$. The molecular dipole moment, denoted by $\vec{\mu}_i(x_i)$, depends on the reaction coordinate x_i .

The solvent and the continuum of electromagnetic modes together constitute the dissipative environment, with the Hamiltonian given by

$$H_E = \sum_k \frac{P_{ck}^2}{2} + \frac{1}{2}\omega_{ck}^2 \left(Q_{ck} + \frac{g_{ck}}{\omega_{ck}^2} x_c \right)^2 + \sum_{i=1}^{N_{\text{mol}}} \sum_k \frac{P_{ik}^2}{2} + \frac{1}{2}\omega_{ik}^2 \left(Q_{ik} + \frac{g_{ik}x_i}{\omega_{ik}^2} \right)^2, \quad (3)$$

where the cavity mode and each molecule are coupled to their respective baths, represented as collections of harmonic oscillators, as schematically illustrated in Fig. 1a. The bath associated with the cavity mode is referred to as the cavity bath, and each molecular bath is referred to as a solvent bath. The k th oscillator in bath α (either cavity or solvent) is described by its momentum $P_{\alpha k}$ and coordinate $Q_{\alpha k}$, with frequency $\omega_{\alpha k}$ and coupling strength $g_{\alpha k}$. The coupling to the system induces a displacement $g_{\alpha k}x_\alpha/\omega_{\alpha k}^2$ in each oscillator's coordinate.

The environmental influence on the system dynamics is fully captured by the time-correlation function

$$C_\alpha(t) = \frac{1}{\pi} \int_{-\infty}^{\infty} \frac{e^{-i\omega t}}{1 - e^{-\beta\omega}} J_\alpha(\omega) d\omega = \sum_{p=1}^{P \rightarrow \infty} \lambda_\alpha^2 \eta_{\alpha p} e^{-i\gamma_{\alpha p} t}, \quad (4)$$

where $\beta = 1/k_B T$ is the inverse temperature, and $J_\alpha(\omega) = \frac{\pi}{2} \sum_k \frac{c_{\alpha k}^2}{\omega_{\alpha k}} \delta(\omega - \omega_{\alpha k})$ is the spectral density function of bath α . This spectral density encodes the coupling-weighted density of states in the frequency domain for each bath. The time correlation function $C_\alpha(t)$ can be expanded analytically or numerically as a series of exponentials.^{70,71} This exponential expansion can be understood as mapping the original bath onto an effective one, which can be truncated efficiently at finite

temperatures. In this effective representation, the bath consists of P dissipative bosonic modes, each with a complex-valued frequency $\gamma_{\alpha p}$ and a component-wise coupling strength $\eta_{\alpha p}$ to the system. The reorganization energy $\lambda_\alpha^2 = \sum_k \frac{g_{\alpha k}^2}{2\omega_{\alpha k}^2}$ quantifies the overall coupling strength between the system and bath α .

Rooted in the HEOM method in twin space for the system,^{72–74} we can formulate a Schrödinger equation as

$$\frac{d|\Psi(t)\rangle}{dt} = -i\mathcal{H}|\Psi(t)\rangle \quad (5)$$

for the extended wavefunction of the composite system

$$|\Psi(t)\rangle \equiv \sum_{\mathbf{n}} \sum_{v_c v'_c \dots v_{N_{\text{mol}}} v'_{N_{\text{mol}}}} C_{v_c v'_c \dots v_{N_{\text{mol}}} v'_{N_{\text{mol}}}}^{\mathbf{n}}(t) |v_c v'_c \dots v_{N_{\text{mol}}} v'_{N_{\text{mol}}}\rangle \otimes |\mathbf{n}\rangle. \quad (6)$$

which includes both the system (cavity and molecules) and the effective baths. Each physical DoF in the system is represented by two independent indices, v_j and v'_j , which arise from the purification of the density matrices. A single operator O_j for the j th system DoF in Hilbert space corresponds to a pair of superoperators in twin space: $\hat{O}_j = O_j \otimes I_j$ and $\tilde{O}_j = I_j \otimes O_j^\dagger$, where I_j is the identity operator for the j th DoF. Further, $|\mathbf{n}\rangle = |\dots n_{\alpha p} \dots\rangle$ represents the Fock state for the effective environmental modes in the number representation, with creation and annihilation operators $b_{\alpha p}^+$ and $b_{\alpha p}$ defined as

$$b_{\alpha p}^+ |\mathbf{n}\rangle = \sqrt{n_{\alpha p} + 1} |\mathbf{n}_{\alpha p}^+\rangle; \quad (7a)$$

$$b_{\alpha p} |\mathbf{n}\rangle = \sqrt{n_{\alpha p}} |\mathbf{n}_{\alpha p}^-\rangle, \quad (7b)$$

where $|\mathbf{n}_{\alpha p}^\pm\rangle = |\dots n_{\alpha p} \pm 1 \dots\rangle$. The super-Hamiltonian \mathcal{H} is non-Hermitian and can be explicitly expressed as

$$\mathcal{H} = \hat{H}_S + \sum_\alpha \lambda_\alpha^2 \hat{x}_\alpha^2 - \hat{H}_S - \sum_\alpha \lambda_\alpha^2 \hat{x}_\alpha^2 - i \sum_\alpha \sum_p \gamma_{\alpha p} b_{\alpha p}^+ b_{\alpha p} + \sum_\alpha \sum_p \lambda_\alpha [(\hat{x}_\alpha - \tilde{x}_\alpha) b_{\alpha p} + (\eta_{\alpha p} \hat{x}_\alpha - \eta_{\alpha p}^* \tilde{x}_\alpha) b_{\alpha p}^+]. \quad (8)$$

By projecting Eq. (5) onto a specific environmental Fock state, we obtain a differential equation for the auxiliary density operator, $\hat{\rho}^{\mathbf{n}}(t) = \langle \mathbf{n} | \Psi(t) \rangle$, which reproduces the standard form of the HEOM method (see a review paper in Ref. 51 and the literature therein). In particular, the reduced system density operator is given by $\rho_S(t) = \rho^{\mathbf{0}}(t) = \langle \mathbf{n} = \mathbf{0} | \Psi(t) \rangle$. In this work, we assume that the system and the environment are initially factorized, so that $\rho(0) = \rho_S(0) \cdot \rho_E(0)$. Additionally, the environment is assumed to be in thermal equilibrium at the moment $t = 0$. This assumption is equivalent to setting the environmental Fock state to the ground state at the initial time in the HEOM formalism.

To facilitate efficient propagation of the Schrödinger equation in Eq. (5), we employ a tree tensor network state solver.⁴⁰ The high-rank coefficient tensor $C_{v_c v'_c \dots v_{N_{\text{mol}}} v'_{N_{\text{mol}}}}^{\mathbf{n}}(t)$ is decomposed as a tree tensor network state, which is a powerful way to handle the complicated tensor structure involved in this system. As an example, a graphical representation of the TTNS

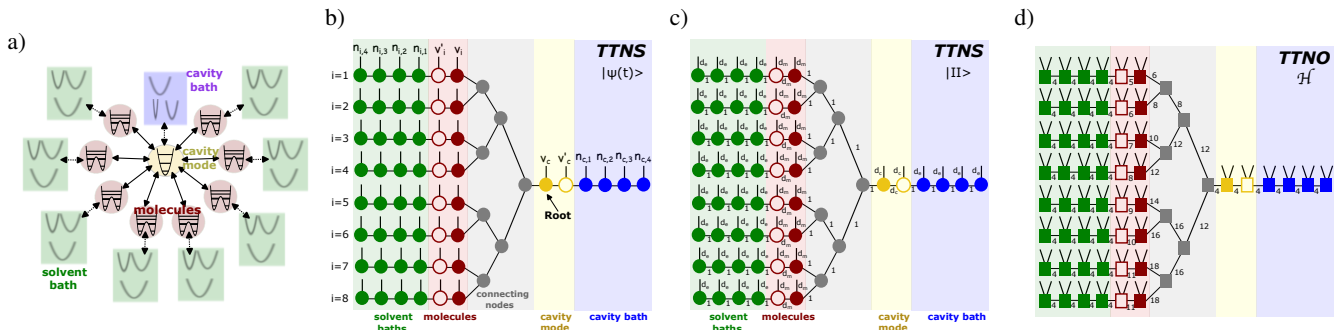


FIG. 1. a) Schematic illustration of an open quantum system model for studying chemical reactions within an optical cavity. The system comprises a single-mode cavity field interacting with N_{mol} molecules. In the illustrated example, $N_{\text{mol}} = 8$. Each molecule is surrounded by a multitude of solvent molecules, while the confined cavity mode is also influenced by far-field radiation modes outside the cavity. b) and c) are graphical representations of a TTNS decomposition of the extended wavefunction $|\Psi(t)\rangle$ and $|\Pi\rangle$, respectively. Each colored circular node in the TTNS represents a low-rank tensor associated with a specific component of the model: molecules (in red), solvent (in green), cavity mode (in yellow), and cavity bath (in blue). Each molecular node is linked to the cavity node through three connecting nodes shown in gray. d) represents a TTNO decomposition of the super-Hamiltonian \mathcal{H} . The square nodes represent the low-rank tensors in the TTNO, and they share the same color-coding scheme as in the TTNS. However, unlike in the TTNS representation, physical nodes in the TTNO have two dangling legs instead of one. The numbers labeled next to the connecting edges specify the bond dimensions of the virtual indices. The parameters d_m , d_c , and d_e indicate the number of basis functions for the vibrational, cavity, and effective environmental DoFs.

decomposition of $|\Psi(t)\rangle$ for a system with $N_{\text{mol}} = 8$ molecules and $P = 4$ effective environmental modes per bath is shown in Fig. 1b. In this decomposition, a node with z -legs corresponds to a rank- z tensor. To achieve an optimal balance between numerical stability, computational efficiency, and simulation time, the number of legs z is constrained to $z \leq 3$.⁶⁰ The physical indices v_c/v'_c (for the cavity), v_i/v'_i (for the molecules), and n_{cp}, n_{ip} (for the effective environmental modes) in $|\Psi(t)\rangle$ are represented by the dangling legs in the yellow (filled/hollow), red (filled/hollow), blue, and green nodes, respectively. The connected legs between neighboring nodes j and k correspond to virtual indices r_{jk} , which runs from 1 to D_{jk} . The maximum value among the bond dimensions $\{D_{jk}\}$ is called the maximal bond dimension D_{max} . In practice, D_{max} is systematically increased until the results converge to a desired accuracy. The gray nodes, which have exclusively connected legs, are termed connecting nodes. The root node is assigned to the filled yellow node for the cavity, which has no parent node. All other nodes, except for the root node, have a parent node. This parent node is the adjacent node on the path pointing toward the root. In the binary tree structure displayed in Fig. 1b, each node has at most two children. The leaves are the nodes without any offspring, representing the termination points of the tree.

The super-Hamiltonian \mathcal{H} can be represented as a tree tensor network operator (TTNO) with the same tree topology as the TTNS used for $|\Psi(t)\rangle$. This decomposition ensures that when the TTNO is applied to the TTNS of $\Psi(t)$, the tree structure is preserved. The construction of the TTNO for \mathcal{H} can be performed in an automatic manner.^{75–78} In this work, we use an optimal TTNO constructor based on bipartite graph theory, which allows for an efficient construction of the TTNO.⁷⁸ The resulting TTNO, corresponding to the tree shape shown in Fig. 1b, is depicted in Fig. 1d. A key difference between the TTNS and the TTNO is that in the TTNO, the physical nodes possess two dangling legs. To evolve Eq. (5), we adopt

a time propagation scheme based on the time-dependent variational principle (TDVP),^{79–84} as detailed in Ref. 40. After solving Eq. (5), observables of interest can be extracted from the wavefunction $|\Psi(t)\rangle$.

For the symmetric double-well model considered in this work, we assume that reactant and product regions are divided by a surface at $x_i^\ddagger = 0$. The population of the i th molecule in the product region is obtained as

$$P_i(t) = \text{Tr}\{h_i\rho(t)\} = \langle \Pi | \hat{h}_i | \Psi(t) \rangle. \quad (9)$$

Here $h_i = \theta(x_i - x_i^\ddagger)$ is the Heaviside projection operator onto the product region, where $x_i > x_i^\ddagger$. The wavefunction $|\Pi\rangle = |1_{\text{sys}}\rangle \otimes |\mathbf{n} = \mathbf{0}\rangle$ corresponds to the state where the system is in a unit vector state in twin space, i.e., $|1_{\text{sys}}\rangle = \otimes_i \sum_{v_i=v'_i} |v_i v'_i\rangle$, and the environmental Fock state is in the ground state.

To perform the inner product in Eq. (9), the wavefunction $|\Pi\rangle$ is also decomposed as a TTNS, maintaining the same tree topology as $|\Psi(t)\rangle$, as displayed in Fig. 1c. The number next to the legs denotes the bond dimension of the corresponding index. The parameters d_m , d_c , and d_e represent the number of basis functions for the molecular reactive DoF, cavity mode, and the effective environmental bosons, respectively. Each node in the TTNS is represented by a rank-3 tensor $V_{i_1 \times i_2 \times i_3}$, where i_1 , i_2 , and i_3 are the dimensions of the respective indices. For the connecting nodes, the tensor is $V_{1 \times 1 \times 1} = 1$. For the molecular (in red) or cavity (in yellow) nodes, the non-zero entries in the tensor are $V_{1 \times d_{m/c} \times d_{m/c}}[1, j, k] = \delta_{jk}$ (filled node) and $V_{d_{m/c} \times 1 \times d_{m/c}}[j, 1, k] = \delta_{jk}$ (hollow node). For the environmental nodes (in green and blue), the non-zero entry is $V_{1 \times 1 \times d_e}[1, 1, 1] = 1$.

The rigorous expression for the first-order reaction rate constant of the i th molecule, moving from the reactant (left well) to the product region (right well), in the flux correlation func-

tion formalism is given by^{85–88}

$$k_i = \lim_{t \rightarrow t_p} k_i(t) = \lim_{t \rightarrow t_p} \frac{C_i^{\text{fs}}(t)}{1 - 2P_i(t)}. \quad (10)$$

Here, t_p is the time at which $k_i(t)$ reaches a plateau. The flux-side correlation function is defined as

$$C_i^{\text{fs}}(t) = \text{Tr}\{\rho(t)F_i\} = \langle \Pi | \tilde{F}_i | \Psi(t) \rangle, \quad (11)$$

where $F_i = i[H, h_i]$ is the flux operator.

In the context of quantum dynamical simulations, it is important to note that the plateau value of $k_i(t)$ in Eq. (10), which corresponds to the reaction rate, is independent of the choice of the initial density matrix. For the calculations in this work, the initial molecular vibrational wavefunction is largely prepared in the reactant region, and the cavity mode is assumed to be in thermal equilibrium. The system density operator is then defined as

$$\rho_S(0) = \left(\prod_{i=1}^{N_{\text{mol}}} \frac{e^{-\frac{\beta H_{\text{mol}}^i}{2}} (1 - h_i) e^{-\frac{\beta H_{\text{mol}}^i}{2}}}{Z_i} \right) \cdot \frac{e^{-\beta H_c(\mathbf{x}=0)}}{\text{Tr}\{e^{-\beta H_c(\mathbf{x}=0)}\}} \quad (12)$$

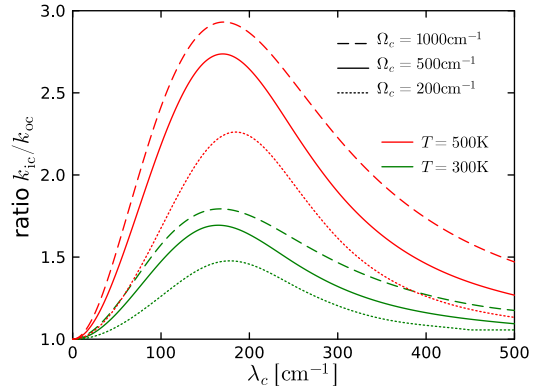
with $Z_i = \text{Tr}_i \left\{ e^{-\frac{\beta H_{\text{mol}}^i}{2}} (1 - h_i) e^{-\frac{\beta H_{\text{mol}}^i}{2}} \right\}$ is a partition function for the i th molecule. The singular value decomposition of the initial density matrix in Eq. (12) is employed to construct the initial tree tensor network state.

In the simulations conducted for this study, the following parameters are used for the double-well model, $E_b = 2250 \text{ cm}^{-1}$ and $a = 44.4 \text{ a.u.}$, which are consistent with previous studies in the field.^{2,31,34–37,74} The Debye-Lorentzian spectral density function is adopted to characterize the baths and their interaction with the system

$$J_\alpha(\omega) = \frac{2\lambda_\alpha^2 \omega \Omega_\alpha}{\omega^2 + \Omega_\alpha^2}, \quad (13)$$

where Ω_α is the characteristic frequency of bath α . All solvent baths share the same parameters, which are fixed as $\lambda_i = 100 \text{ cm}^{-1}$ and $\Omega_i = 200 \text{ cm}^{-1}$. The exponential expansion of the time correlation function in Eq. (4) is performed using the Padé decomposition scheme.⁷⁰ The molecular vibrational DoFs are described by the potential-optimized discrete variable representation,^{89,90} with the lowest d_m eigenstates taken into account. For simplicity, the primary analysis assumes that all molecular dipoles are oriented along the direction of the cavity field polarization, $\vec{\mu}_i(x_i) \cdot \vec{e} = x_i$. The influence of other dipole orientations, including oppositely and anisotropically aligned configurations, is addressed comprehensively in the supplementary information (SI). The cavity mode is represented by the lowest d_c harmonic eigenstates. The convergence is meticulously verified, with careful attention to the following parameters: d_m , d_c , d_e , time step Δt , the number of Padé poles P , and the maximal bond dimension D_{max} . Without further specification, we set $d_m = 6$, $d_c = 10$, $\Delta t = 0.5 \text{ fs}$, $P = 4$, and $D_{\text{max}} = 30$. Depending on the specific parameters, the timescale for $k(t)$ to reach a plateau, t_p , varies between 10ps and 50ps.

a) $\eta_c = 0.00125 \text{ a.u.}$



b) $\eta_c = 0.005 \text{ a.u.}$

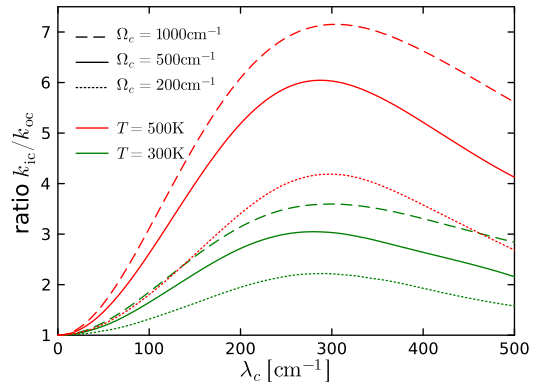


FIG. 2. Ratio of rates k_{ic}/k_{oc} for a single molecule undergoing a reaction inside an optical cavity (k_{ic}) compared to the outside rate (k_{oc}) as a function of the cavity damping strength λ_c . The results for two different temperatures T and three characteristic frequencies Ω_c of the cavity bath, and light-matter coupling strengths ($\eta_c = 0.00125 \text{ a.u.}$ in the upper panel and $\eta_c = 0.005 \text{ a.u.}$ in the lower panel) are shown. The cavity frequency is kept at $\omega_c = 1185 \text{ cm}^{-1}$ and $d_c = 10$.

It is worth noting that while the matrix product state (MPS),⁹¹ also known as tensor train (TT),⁹² is a particular, simpler case of the TTNS, using MPS/TT for simulating reaction dynamics in vibrational polariton chemistry—especially in the collective regime—is computationally inefficient. This inefficiency arises due to the complexity of correlations in such systems, which require more flexible tensor network topologies. Further details on the numerical performance of different tensor network structures are provided in Appendix A.

III. RESULTS

In practice, the cavity is not perfectly reflective and is therefore subject to external noise from the continuum of far-field electromagnetic modes. Previous numerically exact quantum dynamical studies in the single-molecule limit have demonstrated that, in a resonant but lossless cavity, reaction rates remain unaffected.^{1,34,36} Furthermore, an interpolated rate theory at the single-molecule level, based on Fermi's Golden

Rule in both the lossless and lossy limits, which is valid in the Markovian and weak light-matter coupling regime, predicts a turnover in reaction rates inside the cavity as a function of the cavity loss rate.⁹³ These findings give an important hint that cavity leakage may be a crucial factor in altering reaction dynamics inside an optical microcavity. Accordingly, the objective of this work is to understand how ground-state chemical reactions within an optical cavity are influenced by cavity damping. We begin by investigating the effect of cavity damping strength on reaction rate modifications at the single-molecule level, then extend our analysis to the collective regime, where multiple molecules are simultaneously coupled to the cavity mode.

In this work, cavity leakage is modeled by introducing a cavity bath, with the cavity damping strength quantified by the parameter λ_c . This is verified by examining the dynamics of the average photonic excitation number, given by $\langle n_c(t) \rangle = \text{Tr}\{a_c^\dagger a_c \rho(t)\}$. Here, $a_c^\dagger = \sqrt{\omega_c/2}(x_c - ip_c/\omega_c)$ and $a_c = \sqrt{\omega_c/2}(x_c + ip_c/\omega_c)$ represent the creation and annihilation operators of the confined cavity mode, respectively. Detailed data supporting this verification are provided in the SI.

Fig. 2 presents the cavity-induced rate modification, represented as k_{ic}/k_{oc} —the ratio of reaction rates inside and outside the cavity—in the single-molecule limit, plotted as a function of λ_c . The cavity frequency is set at $\omega_c = 1185 \text{ cm}^{-1}$, closely resonant with molecular vibrational transitions and corresponding to the peak in the rate modification profile over ω_c (see also Fig. 3b and Fig. 4b). The rate within the cavity initially increases with λ_c , reaching a maximum before this rate enhancement diminishes as λ_c continues to increase. This behavior is examined with various values of temperature T , the characteristic frequency Ω_c of the cavity bath, and the light-matter coupling strength η_c . The extent of the rate modification depends on temperature, Ω_c , and η_c . Notably, the cavity-induced rate modification is a finite-temperature effect, vanishing at low temperatures and saturating as the temperature rises, as demonstrated in our previous study.¹ Furthermore, the rate modification initially increases with Ω_c , then plateaus, and gradually decreases at higher Ω_c values, as demonstrated in the SI. However, both temperature T and Ω_c only slightly affect the crossover value of λ_c . In contrast, increasing the light-matter coupling strength η_c not only strengthens the rate modification significantly but also shifts the crossover λ_c to a much higher value, rendering the rate modification more resilient to ambient noise. It is worth noting that, in the strong light-matter coupling regime, the inclusion of higher photonic excitation states is critical. Restricting the consideration to only the photonic ground state and first excited state leads not only to incorrect predictions of the resonant peak in the rate modification profile as a function of the cavity frequency ω_c , but also to a significant overestimation of the turnover λ_c . The detailed analysis supporting these findings and a more systematic study of the impact of the light-matter coupling strength on reaction dynamics are provided in the SI.

This observation fits into the notion of the stochastic resonance theory, which was first proposed to explain the periodic recurrence of Earth’s ice ages.^{94,95} Over time, it has pro-

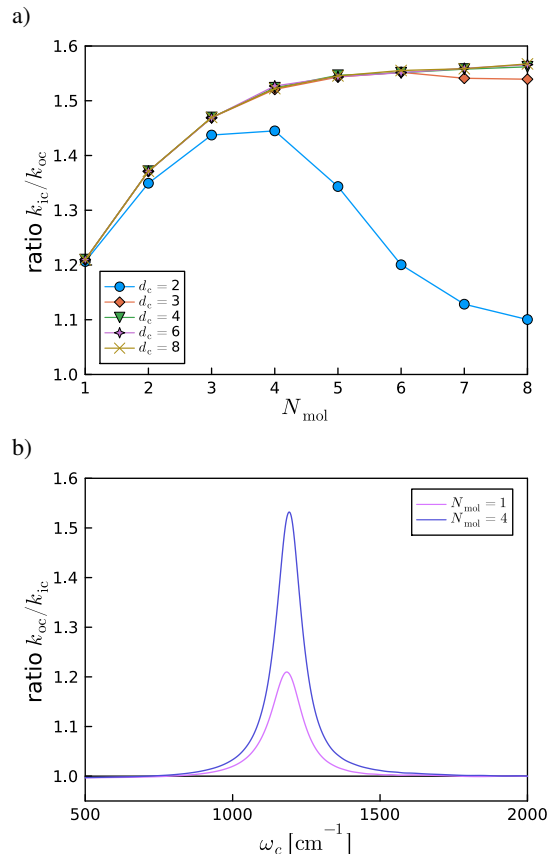


FIG. 3. a) Ratio of rates k_{ic}/k_{oc} as a function of the number of molecules collectively coupled to the cavity mode. Note that k_{ic}/k_{oc} is identical for each individual molecule as the constituent of the molecular ensemble. Results are shown for different numbers of d_c lowest photonic states. The cavity frequency is fixed at $\omega_c = 1185 \text{ cm}^{-1}$. b) Rate modification profile as a function of the cavity frequency for cases with one and four molecules coupled to the cavity mode, respectively, and with $d_c = 6$. Remaining parameters are $\lambda_c = 50 \text{ cm}^{-1}$, $\Omega_c = 1000 \text{ cm}^{-1}$, $\eta_c = 0.00125 \text{ a.u.}$, and $T = 300 \text{ K}$.

pered into a broad field on its own with diverse applications across physics, chemistry, biomedical sciences, engineering, and beyond, highlighting the constructive role of an optimal amount of noise.^{66,96–101} Stochastic resonance refers to a phenomenon where a moderate level of noise improves a system’s sensitivity to detect weak, information-carrying signals.⁶⁶ For chemical reactions inside an optical cavity, three key elements have been possessed for the emergence of stochastic resonance. Firstly, reactions take place in a solvent, which serves as a source of substantial background noise. Secondly, reactive molecules are inherently nonlinear systems that support threshold-like barrier-crossing events. Thirdly, cavity leakage exposes reactions to a generically weak coherent input, which could boost the system’s sensitivity, depending on the noise level.

In many cases, stochastic resonance is observed as a collective effect.^{102,103} For example, it is found that the sensitivity of paddlefish electroreceptors to detect individual plankton is enhanced when plankton form a swarm.¹⁰⁴ Similarly, it is of

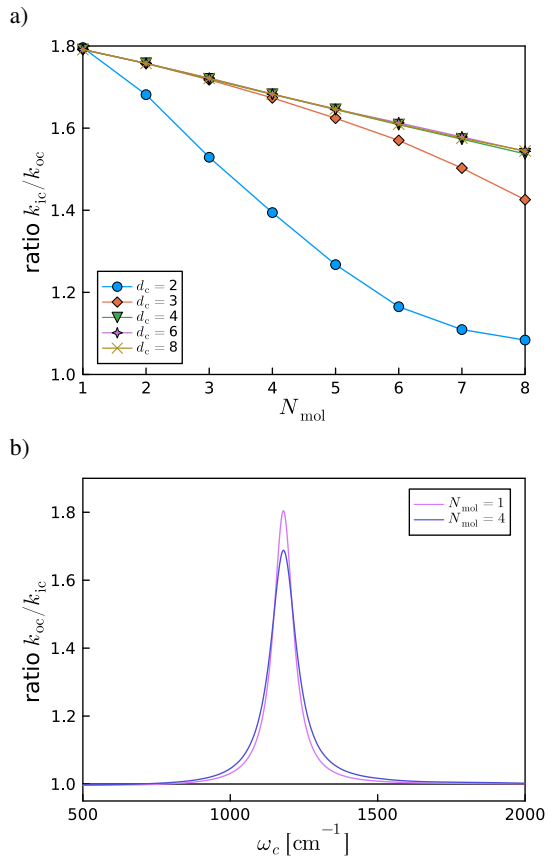


FIG. 4. Same as Fig. 3 except that $\lambda_c = 165 \text{ cm}^{-1}$.

great interest to explore how the reaction dynamics inside the cavity change in the collective regime, by gradually increasing the number of molecules coupled to the cavity mode.

We begin with a weakly-damped cavity mode characterized by $\lambda_c = 50 \text{ cm}^{-1}$, with other parameters set as $T = 300 \text{ K}$ and $\Omega_c = 1000 \text{ cm}^{-1}$. In addition, the light-matter coupling strength per molecule is fixed at $\eta_c = 0.00125 \text{ a.u.}$, meaning that the Rabi splitting Ω_R increases as the number of molecules grows. For a homogeneous molecular aggregate in the all-aligned dipole configuration, the rate ratio k_{ic}/k_{oc} is identical for every individual molecule in the ensemble. In Fig. 3a, we show k_{ic}/k_{oc} as a function of the number of molecules collectively coupled to the cavity mode, with d_c lowest photonic states included in the calculations. As more molecules are coupled through the cavity mode, the reaction rate of an individual molecule as part of the connected molecular network inside the cavity increases, in agreement with the finding in Ref. 35. It is worth noting that, in the collective regime, the involvement of higher photonic excitation manifolds also becomes necessary for accurate results. For the scenario in Fig. 3, at least the two lowest photonic excited states ($d_c = 3$) are required to reach convergence for $N_{mol} \geq 2$, and $d_c = 4$ for $N_{mol} \geq 7$. If only the lowest photonic excited state ($d_c = 2$) is considered, both the reaction rates and the decay of oscillations in the flux-side correlation functions and $\langle n_c(t) \rangle$ are significantly underestimated, as demonstrated in

the SI, suggesting the importance of multi-photon processes in capturing the dissipative nature of the cavity bath, which is crucial for cavity-induced reaction modifications. Furthermore, we observed that as the number of molecules increases from $N_{mol} = 1$ to $N_{mol} = 4$, the height of the resonant peak in the reaction rate modification profile increases, as shown in Fig. 3b, while the peak becomes sharper. Specifically, the full width at half maximum (FWHM) is reduced from approximately 125 cm^{-1} for $N_{mol} = 1$ to 105 cm^{-1} for $N_{mol} = 4$.

In contrast, when the cavity mode is more heavily damped with $\lambda_c = 165 \text{ cm}^{-1}$ while all other parameters remain unchanged, increasing N_{mol} results in a steady drop of k_{ic}/k_{oc} , as shown in Fig. 4a. Additionally, in this scenario, the FWHM of the resonant peak in the cavity-induced rate modification profile broadens from about 80 cm^{-1} for $N_{mol} = 1$ to 105 cm^{-1} for $N_{mol} = 4$, as shown in Fig. 4b. Moreover, with the larger λ_c , more photonic excited states contribute to the collective reaction dynamics within an optical cavity. For instance, $d_c = 4$ photonic states are required for $N_{mol} > 4$, as illustrated in Fig. 4a.

These findings support the hypothesis that cavity-induced rate modifications might also be influenced by factors beyond just the presence of VSC, typically indicated by a large Rabi splitting. Specifically, in the single-molecule limit, the rate modification profile as a function of the cavity frequency ω_c and the absorption spectra (both detailed in the SI) reveal that a sharp resonant peak in the rate modification profile can emerge regardless of whether the Rabi splitting is present or absent. In the VSC regime—characterized by a Rabi splitting that significantly exceeds the full width at half maximum of the split peaks in the absorption spectra—only a broad and weak resonant peak is observed. Our results demonstrate the reaction rate is considerably impacted by the cavity damping strength, which is highly associated with the specifics of the cavity setup, including the material composition and quality factor. In the Markovian regime, it is known that the Rabi splitting Ω_R is proportional to the square root of molecular concentration $\sqrt{N_{mol}/V}$.¹ In the collective coupling scenario, where the Rabi splitting increases with the number of molecules coupled to the cavity mode as we maintain a constant light-matter coupling strength per molecule, the rate changes exhibit diverse trends depending on the cavity damping strength. Further results detailing the ratio of k_{ic}/k_{oc} as a function of N_{mol} for various cavity damping strength λ_c are provided in the SI. These observations suggest that the Rabi splitting alone is not the determining factor for observing rate modification within the cavity. The possibility that the experimental reproducibility challenges in polaritonic chemistry might be related to the delicacy of stochastic resonance was first hinted in Refs. 105 and 106. Our findings in this work may provide an important numerical clue into discrepancies in experimental outcomes.^{4,6,14,15}

We also notice that in the collective coupling regime, while the reaction rate varies with N_{mol} , it does not exceed the maximum rate observed at the single-molecule level under the same conditions of temperature, Ω_c , and η_c . This suggests that studies at the single-molecule level may provide valuable predictions on the upper limit of cavity-induced rate modifica-

tion for a specific chemical reaction in the collective coupling regime.

From another perspective, our results clearly show that the reaction rate for a single molecule, as the building block of a molecular network, can differ significantly from that of an isolated molecule. Moreover, the reaction kinetics of a molecular assembly organized by the cavity mode, in response to a certain level of external noise, are highly sensitive to the system's size. This raises a compelling question: For a macroscopically large ensemble of molecules collectively coupled to a cavity mode, could even a very weak perturbation surrounding the cavity be perceived and amplified throughout the entire connected cavity-molecule system, leading to a drastic change in reaction dynamics? Validating this conjecture will require further investigations, both theoretically and experimentally.

IV. CONCLUSION

In summary, we conduct a quantum dynamical and numerically exact study on the impact of cavity damping strength on condensed-phase chemical reactions inside an optical microcavity under VSC conditions, using the HEOM method with an efficient tree tensor network decomposition scheme. Our results reveal that cavity-induced rate modifications exhibit a typical stochastic resonance feature. Specifically, reaction rates within a cavity are significantly enhanced when the cavity frequency is tuned in resonance with the molecular vibrational transition energy, not only under VSC conditions but also at an intermediate level of cavity damping. Additionally, distinct behaviors are observed as the number of molecules collectively coupled to the cavity mode increases, depending on the cavity damping strength: under weak damping, reaction rates inside the cavity can be boosted as the number of molecules grows, whereas strong damping leads to a decrease in reaction rates with molecular aggregation.

We hope this study will inspire deeper curiosity into the intricacies of vibrational polariton chemistry experiments, and into factors beyond VSC that could potentially lead to major ramifications in the reaction dynamics. It is important to note, however, that a substantial gap remains between the current model study and experimental observations. Looking forward, we plan to develop a more advanced tensor network state approach that extends beyond the tree tensor network topology, allowing us to investigate more realistic multi-mode cavities. We also aim to extend this approach to realistic molecular systems by combining it with the *ab initio* simulations, moving beyond simplified models to more accurately represent experimental conditions.

ACKNOWLEDGMENTS

The author appreciates valuable discussions with Richard Milbradt on the algorithm for constructing a TTNO with state diagrams, and with Prof. Jiushu Shao on the stochastic resonance theory. Y.K. thanks the Swiss National Science Foundation for the award of a research fellowship.

SUPPLEMENTARY INFORMATION

See the supplementary material for the details and further analysis of (1) the impact of cavity bath parameters λ_c and Ω_c on the damping of system dynamics; (2) the impact of bath characteristic frequency Ω_α on reaction dynamics; (3) the impact of the light-matter coupling strength on reaction dynamics; (4) infrared absorption line shapes and rate modification profiles in the single-molecule limit; (5) the importance of higher photonic excitation manifold; (6) the impact of various noise level in collective coupling regime; and (7) the impact of dipole orientations.

DATA AVAILABILITY STATEMENT

The data and code that support the findings of this work are available from the corresponding author upon reasonable request.

Appendix A: Comparison of numerical performances between MPS and TTNS

In this appendix, we demonstrate the advantages of using the TTNS approach over the MPS/TT for studying chemical reactions inside an optical cavity. MPS/TT represents a special, simplified form of TTNS, where all nodes are arranged in a one-dimensional chain, as illustrated in Fig. 5. Although MPS/TT restricts the network topology, its numerical performance is still heavily influenced by the ordering of physical indices. Fig. 5b and Fig. 5c compare $k(t)$ obtained with two different index orderings in the MPS. In the first configuration, molecular nodes and their associated solvent bath nodes are attached subsequently to the cavity and cavity bath nodes on the right. While each molecule couples equally to the cavity mode, the higher-index molecular nodes are positioned farther from the cavity node, giving rise to long-distance entanglement and thus necessitating a considerably large bond dimension to accurately capture the system dynamics. This issue can be partially mitigated by arranging half of the molecular and associated bath nodes on either side of the cavity nodes, as shown in Fig. 5c. Nevertheless, a large bond dimension is still required to obtain smooth and converged results.

In the TTNS decomposition scheme tailored to the collective regime of vibrational polariton chemistry, each molecular node is positioned equidistant from the cavity node, separated by only a few connecting nodes. This tree topology and index arrangement significantly reduce the need for large bond dimensions, optimizing computational efficiency while preserving accuracy. For instance, simulations with a bond dimension of $D_{\max} = 20$ are sufficient to produce high-quality results, as shown in Fig. 5d.

¹T. W. Ebbesen, "Hybrid light-matter states in a molecular and material science perspective," *Acc. Chem. Res.* **49**, 2403–2412 (2016).

²A. Thomas, J. George, A. Shalabney, M. Dryzhakov, S. J. Varma, J. Moran, T. Chervy, X. Zhong, E. Devaux, C. Genet, *et al.*, "Ground-state chemical

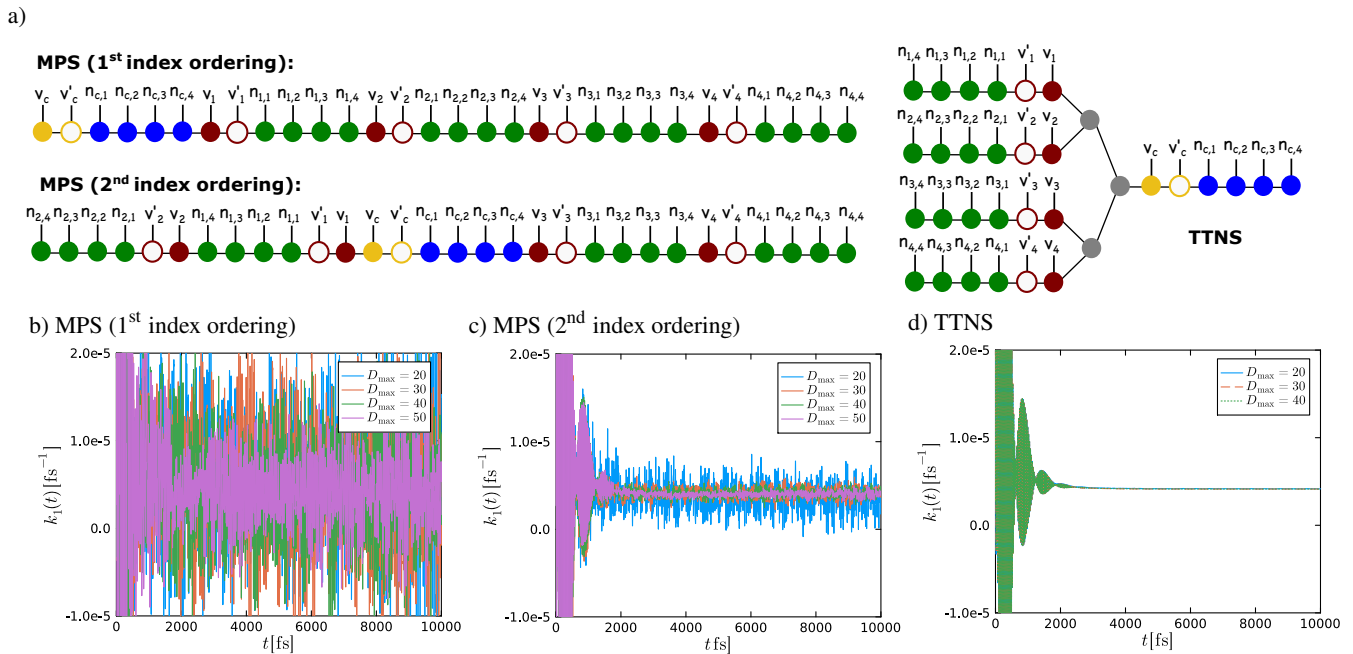


FIG. 5. a) Illustration of MPS/TT decompositions with two different arrangements of physical indices on the left side, and a TTNS decomposition on the right side of the extended wavefunction $|\Psi(t)\rangle$ for $N_{\text{mol}} = 4$. b-d) Rescaled flux-side correlation function $k_1(t)$ for the first molecule, as defined in Eq. (10), is shown with varying maximal bond dimensions. Each panel corresponds to a tensor network state decomposition scheme illustrated in a). Results in c) for $D_{\text{max}} = 20$, $D_{\text{max}} = 30$, and $D_{\text{max}} = 40$ are represented by solid, dashed, and dotted lines, respectively, to avoid visual overlap from superimposition. The pertinent parameters are set as follows: $\omega_c = 1185 \text{ cm}^{-1}$, $\lambda_c = 165 \text{ cm}^{-1}$, $\Omega_c = 1000 \text{ cm}^{-1}$, $\eta_c = 0.00125 \text{ a.u.}$, $d_c = 6$, and $T = 300 \text{ K}$.

- reactivity under vibrational coupling to the vacuum electromagnetic field,” *Angew. Chem.-ger. Edit.* **128**, 11634–11638 (2016).
- ³R. M. Vergauwe, A. Thomas, K. Nagarajan, A. Shalabney, J. George, T. Chervy, M. Seidel, E. Devaux, V. Torbeev, and T. W. Ebbesen, “Modification of enzyme activity by vibrational strong coupling of water,” *Angew. Chem. - Int. Ed.* **58**, 15324–15328 (2019).
- ⁴J. Lather, P. Bhatt, A. Thomas, T. W. Ebbesen, and J. George, “Cavity catalysis by cooperative vibrational strong coupling of reactant and solvent molecules,” *Angew. Chem. - Int. Ed.* **58**, 10635–10638 (2019).
- ⁵A. Thomas, L. Lethuillier-Karl, K. Nagarajan, R. M. Vergauwe, J. George, T. Chervy, A. Shalabney, E. Devaux, C. Genet, J. Moran, et al., “Tilting a ground-state reactivity landscape by vibrational strong coupling,” *Science* **363**, 615–619 (2019).
- ⁶H. Hirata, A. Shalabney, and J. George, “Vacuum-field catalysis: Accelerated reactions by vibrational ultra strong coupling,” *chemRxiv:7234721.v5* (2021).
- ⁷A. Thomas, A. Jayachandran, L. Lethuillier-Karl, R. M. Vergauwe, K. Nagarajan, E. Devaux, C. Genet, J. Moran, and T. W. Ebbesen, “Ground state chemistry under vibrational strong coupling: dependence of thermodynamic parameters on the Rabi splitting energy,” *Proc. Spie.* **9**, 249–255 (2020).
- ⁸K. Hirai, J. A. Hutchison, and H. Uji-i, “Recent progress in vibropolaritonic chemistry,” *ChemPlusChem* **85**, 1981–1988 (2020).
- ⁹K. Hirai, R. Takeda, J. A. Hutchison, and H. Uji-i, “Modulation of Prins cyclization by vibrational strong coupling,” *Angew. Chem.-ger. Edit.* **132**, 5370–5373 (2020).
- ¹⁰A. Sau, K. Nagarajan, B. Patrauhau, L. Lethuillier-Karl, R. M. Vergauwe, A. Thomas, J. Moran, C. Genet, and T. W. Ebbesen, “Modifying Woodward–Hoffmann stereoselectivity under vibrational strong coupling,” *Angew. Chem. - Int. Ed.* **60**, 5712–5717 (2021).
- ¹¹J. Lather, A. N. Thabassum, J. Singh, and J. George, “Cavity catalysis: modifying linear free-energy relationship under cooperative vibrational strong coupling,” *Chem. Sci.* **13**, 195–202 (2022).
- ¹²W. Ahn, J. F. Triana, F. Recabal, F. Herrera, and B. S. Simpkins, “Modification of ground-state chemical reactivity via light–matter coherence in infrared cavities,” *Science* **380**, 1165–1168 (2023).
- ¹³T. Ebbesen, B. Patrauhau, M. Piejko, R. Mayer, C. Antheaume, T. Sangchai, G. Ragazzon, A. Jayachandran, E. Devaux, C. Genet, et al., “Direct observation of polaritonic chemistry by nuclear magnetic resonance spectroscopy,” (2023).
- ¹⁴M. V. Imperatore, J. B. Asbury, and N. C. Giebink, “Reproducibility of cavity-enhanced chemical reaction rates in the vibrational strong coupling regime,” *J. Chem. Phys.* **154** (2021).
- ¹⁵G. D. Wiesehan and W. Xiong, “Negligible rate enhancement from reported cooperative vibrational strong coupling catalysis,” *J. Chem. Phys.* **155** (2021).
- ¹⁶J. Galego, F. J. Garcia-Vidal, and J. Feist, “Suppressing photochemical reactions with quantized light fields,” *Nat. Commun.* **7**, 13841 (2016).
- ¹⁷J. Galego, F. J. Garcia-Vidal, and J. Feist, “Many-molecule reaction triggered by a single photon in polaritonic chemistry,” *Phys. Rev. Lett.* **119**, 136001 (2017).
- ¹⁸J. Galego, C. Climent, F. J. Garcia-Vidal, and J. Feist, “Cavity Casimir-Polder forces and their effects in ground-state chemical reactivity,” *Phys. Rev. X* **9**, 021057 (2019).
- ¹⁹J. A. Campos-Gonzalez-Angulo and J. Yuen-Zhou, “Polaritonic normal modes in transition state theory,” *J. Chem. Phys.* **152**, 161101 (2020).
- ²⁰A. Mandal, S. Montillo Vega, and P. Huo, “Polarized fock states and the dynamical Casimir effect in molecular cavity quantum electrodynamics,” *J. Phys. Chem. Lett.* **11**, 9215–9223 (2020).
- ²¹P.-Y. Yang and J. Cao, “Quantum effects in chemical reactions under polaritonic vibrational strong coupling,” *J. Phys. Chem. Lett.* **12**, 9531–9538 (2021).
- ²²X. Li, A. Mandal, and P. Huo, “Theory of mode-selective chemistry through polaritonic vibrational strong coupling,” *J. Phys. Chem. Lett.* **12**, 6974–6982 (2021).
- ²³T. E. Li, A. Nitzan, and J. E. Subotnik, “On the origin of ground-state vacuum-field catalysis: Equilibrium consideration,” *J. Chem. Phys.* **152**, 234107 (2020).
- ²⁴X. Li, A. Mandal, and P. Huo, “Cavity frequency-dependent theory for

- vibrational polariton chemistry,” *Nat. Commun.* **12**, 1315 (2021).
- ²⁵J. Sun and O. Vendrell, “Suppression and enhancement of thermal chemical rates in a cavity,” *J. Phys. Chem. Lett.* **13**, 4441–4446 (2022).
- ²⁶C. Schäfer, J. Flick, E. Ronca, P. Narang, and A. Rubio, “Shining light on the microscopic resonant mechanism responsible for cavity-mediated chemical reactivity,” *Nat. Commun.* **13**, 7817 (2022).
- ²⁷A. Mandal, X. Li, and P. Huo, “Theory of vibrational polariton chemistry in the collective coupling regime,” *J. Chem. Phys.* **156** (2022).
- ²⁸L. P. Lindoy, A. Mandal, and D. R. Reichman, “Resonant cavity modification of ground-state chemical kinetics,” *J. Phys. Chem. Lett.* **13**, 6580–6586 (2022).
- ²⁹D. S. Wang, T. Neuman, S. F. Yelin, and J. Flick, “Cavity-modified unimolecular dissociation reactions via intramolecular vibrational energy redistribution,” *J. Phys. Chem. Lett.* **13**, 3317–3324 (2022).
- ³⁰E. W. Fischer, J. Anders, and P. Saalfrank, “Cavity-altered thermal isomerization rates and dynamical resonant localization in vibro-polaritonic chemistry,” *J. Chem. Phys.* **156**, 154305 (2022).
- ³¹M. R. Fiechter, J. E. Runeson, J. E. Lawrence, and J. O. Richardson, “How quantum is the resonance behavior in vibrational polariton chemistry?” *J. Phys. Chem. Lett.* **14**, 8261–8267 (2023).
- ³²I. Sokolovskii and G. Groenhof, “Non-Hermitian molecular dynamics simulations of exciton-polaritons in lossy cavities,” *J. Chem. Phys.* **160**, 092501 (2024).
- ³³F. Pavošević, R. L. Smith, and A. Rubio, “Computational study on the catalytic control of endo/exo Diels-Alder reactions by cavity quantum vacuum fluctuations,” *Nat. Commun.* **14**, 2766 (2023).
- ³⁴L. P. Lindoy, A. Mandal, and D. R. Reichman, “Quantum dynamical effects of vibrational strong coupling in chemical reactivity,” *Nat. Commun.* **14**, 2733 (2023).
- ³⁵L. P. Lindoy, A. Mandal, and D. R. Reichman, “Investigating the collective nature of cavity-modified chemical kinetics under vibrational strong coupling,” *Nanophotonics* **13**, 2617–2633 (2024).
- ³⁶W. Ying and P. Huo, “Resonance theory and quantum dynamics simulations of vibrational polariton chemistry,” *J. Chem. Phys.* **159**, 084104 (2023).
- ³⁷D. Hu, W. Ying, and P. Huo, “Resonance enhancement of vibrational polariton chemistry obtained from the mixed quantum-classical dynamics simulations,” *J. Phys. Chem. Lett.* **14**, 11208–11216 (2023).
- ¹Y. Ke and J. O. Richardson, “Insights into the mechanisms of optical cavity-modified ground-state chemical reactions,” *J. Chem. Phys.* **160**, 224704 (2024).
- ²Y. Ke and J. O. Richardson, “Quantum nature of reactivity modification in vibrational polariton chemistry,” *J. Chem. Phys.* **161**, 054104 (2024).
- ⁴⁰Y. Ke, “Tree tensor network state approach for solving hierarchical equations of motion,” *J. Chem. Phys.* **158**, 211102 (2023).
- ⁴¹Y. Tanimura and R. Kubo, “Time evolution of a quantum system in contact with a nearly Gaussian-Markoffian noise bath,” *J. Phys. Soc. Jpn.* **58**, 101–114 (1989).
- ⁴²Y.-a. Yan, F. Yang, Y. Liu, and J. Shao, “Hierarchical approach based on stochastic decoupling to dissipative systems,” *Chem. Phys. Lett.* **395**, 216–221 (2004).
- ⁴³A. Ishizaki and Y. Tanimura, “Quantum dynamics of system strongly coupled to low-temperature colored noise bath: Reduced hierarchy equations approach,” *J. Phys. Soc. Jpn.* **74**, 3131–3134 (2005).
- ⁴⁴R.-X. Xu and Y. Yan, “Dynamics of quantum dissipation systems interacting with bosonic canonical bath: Hierarchical equations of motion approach,” *Phys. Rev. E* **75**, 031107 (2007).
- ⁴⁵Q. Shi, L. Chen, G. Nan, R.-X. Xu, and Y. Yan, “Efficient hierarchical liouville space propagator to quantum dissipative dynamics,” *J. Chem. Phys.* **130**, 084105 (2009).
- ⁴⁶Y. Yan, “Theory of open quantum systems with bath of electrons and phonons and spins: Many-dissipaton density matrixes approach,” *J. Chem. Phys.* **140**, 054105 (2014).
- ⁴⁷J. Jin, X. Zheng, and Y. Yan, “Exact dynamics of dissipative electronic systems and quantum transport: Hierarchical equations of motion approach,” *J. Chem. Phys.* **128**, 234703 (2008).
- ⁴⁸C. Schinabeck, R. Härtle, and M. Thoss, “Hierarchical quantum master equation approach to electronic-vibrational coupling in nonequilibrium transport through nanosystems: Reservoir formulation and application to vibrational instabilities,” *Phys. Rev. B* **97**, 235429 (2018).
- ⁴⁹C.-Y. Hsieh and J. Cao, “A unified stochastic formulation of dissipative quantum dynamics. i. generalized hierarchical equations,” *J. Chem. Phys.* **148**, 014103 (2018).
- ⁵⁰Q. Shi, Y. Xu, Y. Yan, and M. Xu, “Efficient propagation of the hierarchical equations of motion using the matrix product state method,” *J. Chem. Phys.* **148**, 174102 (2018).
- ⁵¹Y. Tanimura, “Numerically “exact” approach to open quantum dynamics: The hierarchical equations of motion (HEOM),” *J. Chem. Phys.* **153**, 020901 (2020).
- ⁵²Y.-Y. Shi, L.-M. Duan, and G. Vidal, “Classical simulation of quantum many-body systems with a tree tensor network,” *Phys. Rev. A* **74**, 022320 (2006).
- ⁵³L. Tagliacozzo, G. Evenbly, and G. Vidal, “Simulation of two-dimensional quantum systems using a tree tensor network that exploits the entropic area law,” *Phys. Rev. B* **80**, 235127 (2009).
- ⁵⁴V. Murg, F. Verstraete, Ö. Legeza, and R. M. Noack, “Simulating strongly correlated quantum systems with tree tensor networks,” *Phys. Rev. B* **82**, 205105 (2010).
- ⁵⁵W. Li, J. von Delft, and T. Xiang, “Efficient simulation of infinite tree tensor network states on the bethe lattice,” *Phys. Rev. B* **86**, 195137 (2012).
- ⁵⁶H. J. Changlani, S. Ghosh, C. L. Henley, and A. M. Läuchli, “Heisenberg antiferromagnet on cayley trees: Low-energy spectrum and even/odd site imbalance,” *Phys. Rev. B* **87**, 085107 (2013).
- ⁵⁷N. Nakatani and G. K.-L. Chan, “Efficient tree tensor network states (TTNS) for quantum chemistry: Generalizations of the density matrix renormalization group algorithm,” *J. Chem. Phys.* **138**, 134113 (2013).
- ⁵⁸C. Lubich, T. Rohwedder, R. Schneider, and B. Vandereycken, “Dynamical approximation by hierarchical Tucker and tensor-train tensors,” *SIAM J. Matrix Anal. Appl.* **34**, 470–494 (2013).
- ⁵⁹V. Murg, F. Verstraete, R. Schneider, P. R. Nagy, and O. Legeza, “Tree tensor network state with variable tensor order: An efficient multireference method for strongly correlated systems,” *J. Chem. Theory Comput.* **11**, 1027–1036 (2015).
- ⁶⁰K. Gunst, F. Verstraete, S. Wouters, O. Legeza, and D. Van Neck, “T3NS: Three-legged tree tensor network states,” *J. Chem. Theory Comput.* **14**, 2026–2033 (2018).
- ⁶¹F. A. Schröder, D. H. Turban, A. J. Musser, N. D. Hine, and A. W. Chin, “Tensor network simulation of multi-environmental open quantum dynamics via machine learning and entanglement renormalisation,” *Nat. Commun.* **10**, 1–10 (2019).
- ⁶²H. R. Larsson, “Computing vibrational eigenstates with tree tensor network states (TTNS),” *J. Chem. Phys.* **151**, 204102 (2019).
- ⁶³G. Ferrari, G. Magnifico, and S. Montangero, “Adaptive-weighted tree tensor networks for disordered quantum many-body systems,” *Phys. Rev. B* **105**, 214201 (2022).
- ⁶⁴S. Montangero, E. Rico, and P. Silvi, “Loop-free tensor networks for high-energy physics,” *Philos. Trans. R. Soc. A* **380**, 20210065 (2022).
- ⁶⁵D. Sulz, C. Lubich, G. Ceruti, I. Lesanovsky, and F. Carollo, “Numerical simulation of long-range open quantum many-body dynamics with tree tensor networks,” *Phys. Rev. A* **109**, 022420 (2024).
- ⁶⁶L. Gammaitoni, P. Hänggi, P. Jung, and F. Marchesoni, “Stochastic resonance,” *Rev. Mod. Phys.* **70**, 223 (1998).
- ⁶⁷J. Flick, M. Ruggenthaler, H. Appel, and A. Rubio, “Atoms and molecules in cavities, from weak to strong coupling in quantum-electrodynamics (QED) chemistry,” *Proc. Natl. Acad. Sci. USA* **114**, 3026–3034 (2017).
- ⁶⁸V. Rokaj, D. M. Welakuh, M. Ruggenthaler, and A. Rubio, “Light–matter interaction in the long-wavelength limit: no ground-state without dipole self-energy,” *J. Phys. B: At. Mol. Opt. Phys.* **51**, 034005 (2018).
- ⁶⁹A. Mandal, M. A. Taylor, B. M. Weight, E. R. Koessler, X. Li, and P. Huo, “Theoretical advances in polariton chemistry and molecular cavity quantum electrodynamics,” *Chem. Rev.* **123**, 9786–9879 (2023).
- ⁷⁰J. Hu, R.-X. Xu, and Y. Yan, “Communication: Padé spectrum decomposition of Fermi function and Bose function,” *J. Chem. Phys.* **133**, 101106 (2010).
- ⁷¹M. Xu, Y. Yan, Q. Shi, J. Ankerhold, and J. Stockburger, “Taming quantum noise for efficient low temperature simulations of open quantum systems,” *Phys. Rev. Lett.* **129**, 230601 (2022).
- ⁷²R. Borrelli, “Density matrix dynamics in twin-formulation: An efficient methodology based on tensor-train representation of reduced equations of motion,” *J. Chem. Phys.* **150**, 234102 (2019).
- ⁷³R. Borrelli and M. F. Gelin, “Finite temperature quantum dynamics of com-

- plex systems: Integrating thermo-field theories and tensor-train methods,” *WIREs Comput Mol Sci*, e1539 (2021).
- ⁷⁴Y. Ke, R. Borrelli, and M. Thoss, “Hierarchical equations of motion approach to hybrid fermionic and bosonic environments: Matrix product state formulation in twin space,” *J. Chem. Phys.* **156**, 194102 (2022).
- ⁷⁵R. M. Milbradt, Q. Huang, and C. B. Mendl, “State diagrams to determine tree tensor network operators,” *SciPost Phys. Core* **7**, 036 (2024).
- ⁷⁶R. M. Milbradt, Q. Huang, and C. B. Mendl, “PyTreeNet: A python library for easy utilisation of tree tensor networks,” arXiv preprint arXiv:2407.13249 (2024).
- ⁷⁷G. Ceruti, D. Kressner, and D. Sulz, “Low-rank tree tensor network operators for long-range pairwise interactions,” arXiv preprint arXiv:2405.09952 (2024).
- ⁷⁸W. Li, J. Ren, H. Yang, H. Wang, and Z. Shuai, “Optimal tree tensor network operators for tensor network simulations: Applications to open quantum systems,” *J. Chem. Phys.* **161**, 054116 (2024).
- ⁷⁹J. Haegeman, C. Lubich, I. Oseledets, B. Vandereycken, and F. Verstraete, “Unifying time evolution and optimization with matrix product states,” *Phys. Rev. B* **94**, 165116 (2016).
- ⁸⁰S. Paecel, T. Köhler, A. Swoboda, S. R. Manmana, U. Schollwöck, and C. Hubig, “Time-evolution methods for matrix-product states,” *Ann. Phys. (NY)* **411**, 167998 (2019).
- ⁸¹A. J. Dunnett and A. W. Chin, “Efficient bond-adaptive approach for finite-temperature open quantum dynamics using the one-site time-dependent variational principle for matrix product states,” *Phys. Rev. B* **104**, 214302 (2021).
- ⁸²D. Bauernfeind and M. Aichhorn, “Time dependent variational principle for tree tensor networks,” *SciPost Physics* **8**, 024 (2020).
- ⁸³B. Kloss, D. Reichman, and Y. Bar Lev, “Studying dynamics in two-dimensional quantum lattices using tree tensor network states,” *SciPost Physics* **9**, 070 (2020).
- ⁸⁴G. Ceruti, C. Lubich, and H. Walach, “Time integration of tree tensor networks,” *SIAM J. Numer. Anal.* **59**, 289–313 (2021).
- ⁸⁵W. H. Miller, S. D. Schwartz, and J. W. Tromp, “Quantum mechanical rate constants for bimolecular reactions,” *J. Chem. Phys.* **79**, 4889–4898 (1983).
- ⁸⁶I. R. Craig, M. Thoss, and H. Wang, “Proton transfer reactions in model condensed-phase environments: Accurate quantum dynamics using the multilayer multiconfiguration time-dependent Hartree approach,” *J. Chem. Phys.* **127**, 144503 (2007).
- ⁸⁷L. Chen and Q. Shi, “Quantum rate dynamics for proton transfer reactions in condensed phase: The exact hierarchical equations of motion approach,” *J. Chem. Phys.* **130**, 134505 (2009).
- ⁸⁸Y. Ke, C. Kaspar, A. Erpenbeck, U. Peskin, and M. Thoss, “Nonequilibrium reaction rate theory: Formulation and implementation within the hierarchical equations of motion approach,” *J. Chem. Phys.* **157**, 034103 (2022).
- ⁸⁹D. T. Colbert and W. H. Miller, “A novel discrete variable representation for quantum mechanical reactive scattering via the S-matrix Kohn method,” *J. Chem. Phys.* **96**, 1982–1991 (1992).
- ⁹⁰J. Echave and D. C. Clary, “Potential optimized discrete variable representation,” *Chem. Phys. Lett.* **190**, 225–230 (1992).
- ⁹¹U. Schollwöck, “The density-matrix renormalization group in the age of matrix product states,” *Ann. Phys. (NY)* **326**, 96–192 (2011).
- ⁹²I. V. Oseledets, “Tensor-train decomposition,” *SIAM J. Sci. Comput.* **33**, 2295–2317 (2011).
- ⁹³W. Ying and P. Huo, “Resonance theory of vibrational strong coupling enhanced polariton chemistry and the role of photonic mode lifetime,” *Commun. Mater.* **5**, 110 (2024).
- ⁹⁴R. Benzi, A. Sutera, and A. Vulpiani, “The mechanism of stochastic resonance,” *J. Phys. A: Math. Gen.* **14**, L453 (1981).
- ⁹⁵C. Nicolis, “Solar variability and stochastic effects on climate,” *Sol. Phys.* **74**, 473–478 (1981).
- ⁹⁶K. Wiesenfeld and F. Moss, “Stochastic resonance and the benefits of noise: from ice ages to crayfish and squids,” *Nature* **373**, 33–36 (1995).
- ⁹⁷B. Andò and S. Graziani, *Stochastic resonance: theory and applications* (Springer Science & Business Media, 2000).
- ⁹⁸P. Hänggi, “Stochastic resonance in biology how noise can enhance detection of weak signals and help improve biological information processing,” *ChemPhysChem* **3**, 285–290 (2002).
- ⁹⁹G. P. Harmer, B. R. Davis, and D. Abbott, “A review of stochastic resonance: Circuits and measurement,” *IEEE Trans. Instrum. Meas.* **51**, 299–309 (2002).
- ¹⁰⁰T. Wellens, V. Shatokhin, and A. Buchleitner, “Stochastic resonance,” *Rep. Prog. Phys.* **67**, 45 (2003).
- ¹⁰¹F. Moss, L. M. Ward, and W. G. Sannita, “Stochastic resonance and sensory information processing: a tutorial and review of application,” *Clin. Neurophysiol.* **115**, 267–281 (2004).
- ¹⁰²P. Jung, U. Behn, E. Pantazelou, and F. Moss, “Collective response in globally coupled bistable systems,” *Phys. Rev. A* **46**, R1709 (1992).
- ¹⁰³J. F. Lindner, B. K. Meadows, W. L. Ditto, M. E. Inchiosa, and A. R. Bulsara, “Array enhanced stochastic resonance and spatiotemporal synchronization,” *Phys. Rev. Lett.* **75**, 3 (1995).
- ¹⁰⁴D. F. Russell, L. A. Wilkens, and F. Moss, “Use of behavioural stochastic resonance by paddle fish for feeding,” *Nature* **402**, 291–294 (1999).
- ¹⁰⁵D. Sidler, M. Ruggenthaler, C. Schäfer, E. Ronca, and A. Rubio, “A perspective on ab initio modeling of polaritonic chemistry: The role of non-equilibrium effects and quantum collectivity,” *J. Chem. Phys.* **156**, 230901 (2022).
- ¹⁰⁶M. Ruggenthaler, D. Sidler, and A. Rubio, “Understanding polaritonic chemistry from ab initio quantum electrodynamics,” *Chem. Rev.* **123**, 11191–11229 (2023).

Supplementary information: Stochastic resonance in vibrational polariton chemistry

IMPACT OF CAVITY BATH PARAMETERS λ_c AND Ω_c ON THE DAMPING OF SYSTEM DYNAMICS

To elucidate the influence of cavity bath parameters on system dynamics, Fig. S1 presents the rescaled flux-side correlation function $k(t)$, and the time evolution of the average photonic excitation number $\langle n_c(t) \rangle$, for various values of λ_c and Ω_c . In Fig. S1a and Fig. S1b, Ω_c is varied while λ_c is held constant at 50 cm^{-1} . Under this condition, variations in Ω_c do not significantly affect the damping rates of either the molecular vibrational or cavity photonic dynamics. In comparison, Fig. S1c and Fig. S1d depict results for varying λ_c with $\Omega_c = 1000 \text{ cm}^{-1}$, where both $k(t)$ and $\langle n_c(t) \rangle$ exhibit accelerated damping as λ_c increases. These findings justify the use of parameter λ_c in this work as a quantifier of the cavity damping strength.

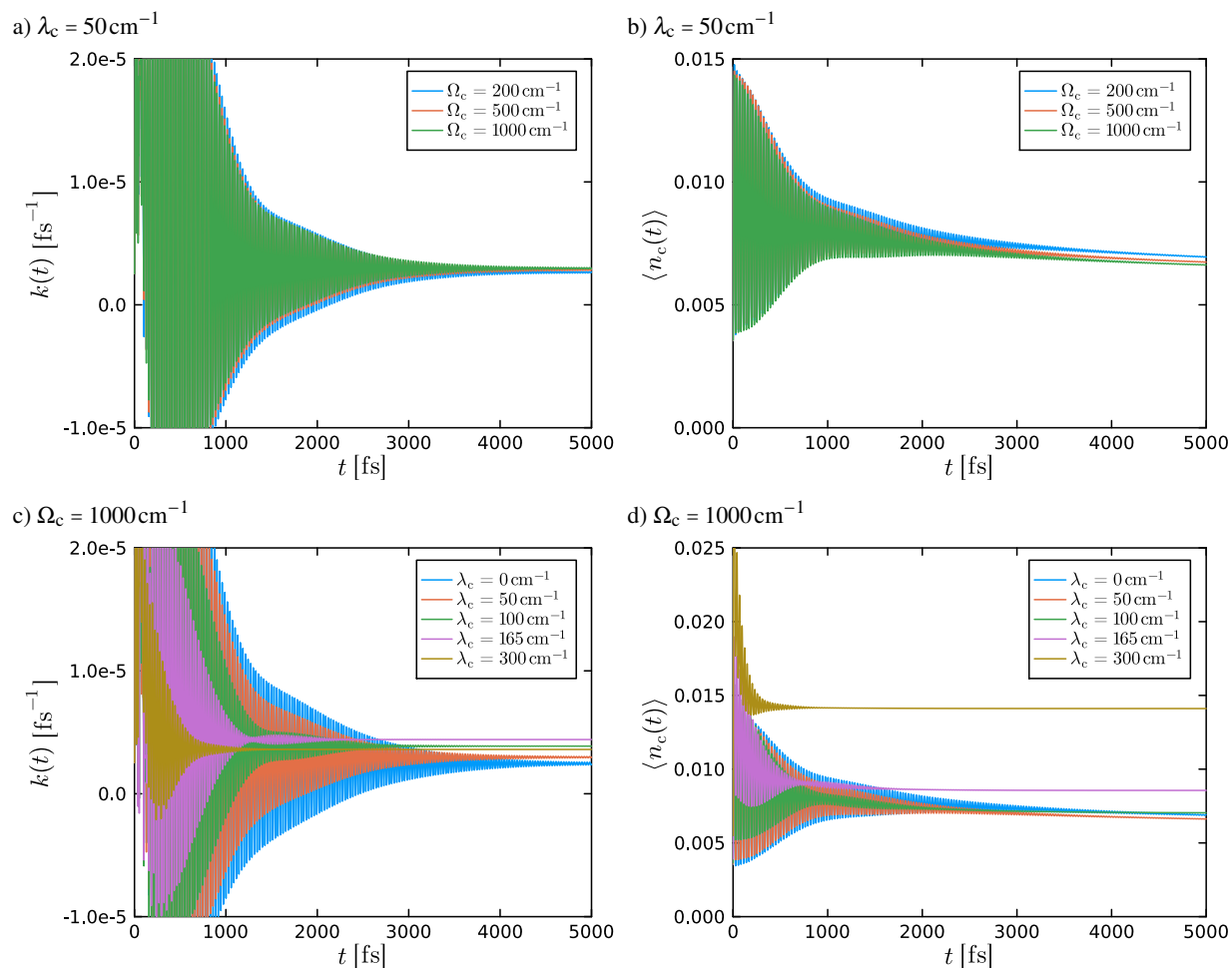


FIG. S1. Rescaled flux-side correlation function $k(t)$, and the dynamics of the average photonic excitation number $\langle n_c(t) \rangle$, are illustrated for different values of Ω_c with $\lambda_c = 50 \text{ cm}^{-1}$ in (a) and (b), respectively. Similarly, the behavior for varying λ_c with a fixed $\Omega_c = 1000 \text{ cm}^{-1}$ is shown in (c) and (d). Other parameters are set as follows: $\omega_c = 1185 \text{ cm}^{-1}$, $\eta_c = 0.00125 \text{ a.u.}$, $T = 300 \text{ K}$, $d_c = 10$, and $N_{\text{mol}} = 1$.

IMPACT OF BATH CHARACTERISTIC FREQUENCY Ω_α ON REACTION DYNAMICS

In this work, the spectral density functions of both the cavity bath and solvent baths are modeled using a Debye-Lorentzian form, characterized by the parameters λ_α and Ω_α . The characteristic frequency Ω_α defines both the peak position and the width of the spectral density function, with a maximum value of $J(\Omega_\alpha) = \lambda_\alpha^2$, as depicted in Fig. S2a.

For the cavity bath, increasing Ω_c initially enhances the reaction rate inside the cavity, followed by a plateau and a gradual decrease at higher Ω_c values, as shown in Fig. S2b. Moreover, the reaction dynamics are also influenced by the characteristic

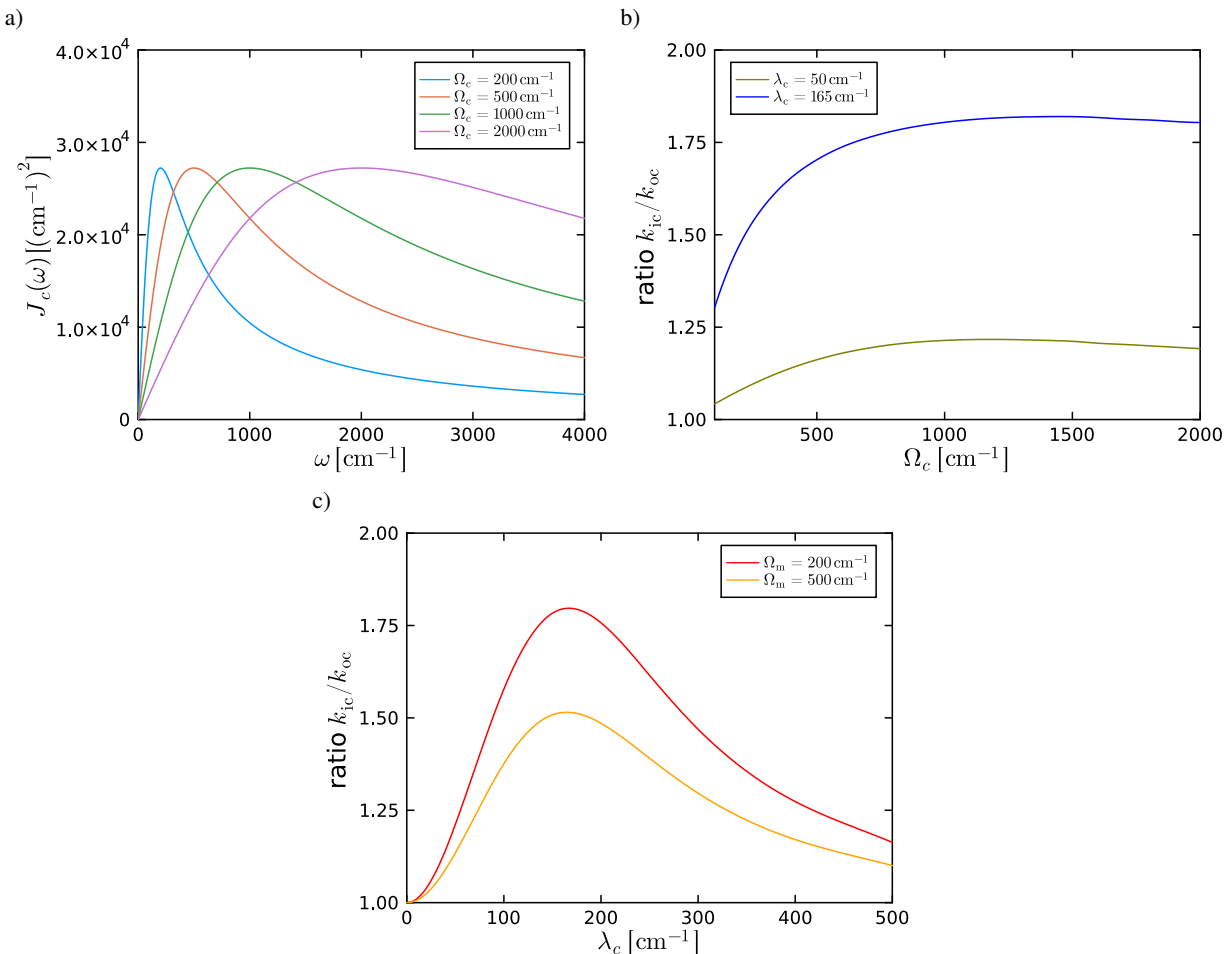


FIG. S2. a) Spectral density function of the cavity bath is shown for $\lambda_c = 100 \text{ cm}^{-1}$ with three different values of the characteristic frequency Ω_c , highlighting how Ω_c influences the peak and width of the function. b) Ratio of rate k_{ic}/k_{oc} as a function of Ω_c for two distinct values of λ_c . These simulations use $P = 6$ Padé poles. c) Ratio of rate k_{ic}/k_{oc} as a function of λ_c for a fixed $\Omega_c = 1000 \text{ cm}^{-1}$ and two different values of the solvent bath characteristic frequency, Ω_m . Other parameters used in the simulations are $\omega_c = 1185 \text{ cm}^{-1}$, $\eta_c = 0.00125 \text{ a.u.}$, $T = 300 \text{ K}$, $d_c = 10$, and $N_{\text{mol}} = 1$.

frequency of the solvent bath, Ω_m . A larger Ω_m increases the reaction rate outside the cavity. For example, the rate k_{oc} rises from $2.46 \times 10^{-6} \text{ fs}^{-1}$ at $\Omega_m = 200 \text{ cm}^{-1}$ to $3.8 \times 10^{-6} \text{ fs}^{-1}$ at $\Omega_m = 500 \text{ cm}^{-1}$. In contrast, a larger Ω_m results in less pronounced changes in the rates inside the cavity, while preserving the stochastic resonance feature, i.e. the turnover of k_{ic}/k_{oc} versus λ_c , as illustrated in Fig. S2c. These findings highlight the differential effects of Ω_α on reaction rates, depending on the bath's nature.

IMPACT OF THE LIGHT-MATTER COUPLING STRENGTH ON REACTION DYNAMICS

In the main text, it is observed that increasing the light-matter coupling strength, η_c , shifts the peak position in the k_{ic}/k_{oc} versus λ_c profile to a larger value and simultaneously increases the peak height. To systematically demonstrate the impact of light-matter coupling strength, Fig. S3 presents the cavity-induced rate modification k_{ic}/k_{oc} as a function of η_c for varying cavity damping strengths. The cavity frequency is fixed at $\omega_c = 1185 \text{ cm}^{-1}$, near resonance with vibrational transitions, and other parameters are $T = 300 \text{ K}$ and $\Omega_c = 1000 \text{ cm}^{-1}$. Interestingly, the reaction rates exhibit a turnover behavior as η_c increases. In a weakly damped cavity ($\lambda_c = 50 \text{ cm}^{-1}$), the maximum rate ratio is $k_{ic}/k_{oc} = 1.225$, occurring at $\eta_c = 0.0025 \text{ a.u.}$ At higher noise levels (larger λ_c), while the rate enhancement inside the cavity is initially suppressed in the small light-matter coupling regime, it increases rapidly with stronger light-matter coupling strength. The maximum rate at higher λ_c is significantly greater than that at lower λ_c . For instance, at $\lambda_c = 300 \text{ cm}^{-1}$, the rate inside the cavity can be enhanced by a factor of 3.8 with a strong light-matter coupling strength $\eta_c = 0.008 \text{ a.u.}$

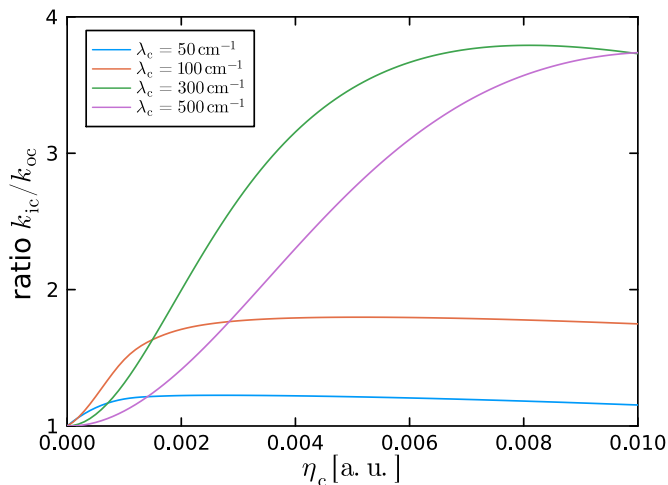


FIG. S3. Ratio of rates k_{i_c}/k_{o_c} as a function of the light-matter coupling strength η_c in the single molecule limit for varying values of λ_c . Other parameters used in the simulations are $\omega_c = 1185 \text{ cm}^{-1}$, $\Omega_c = 1000 \text{ cm}^{-1}$, $T = 300 \text{ K}$, and $d_c = 10$.

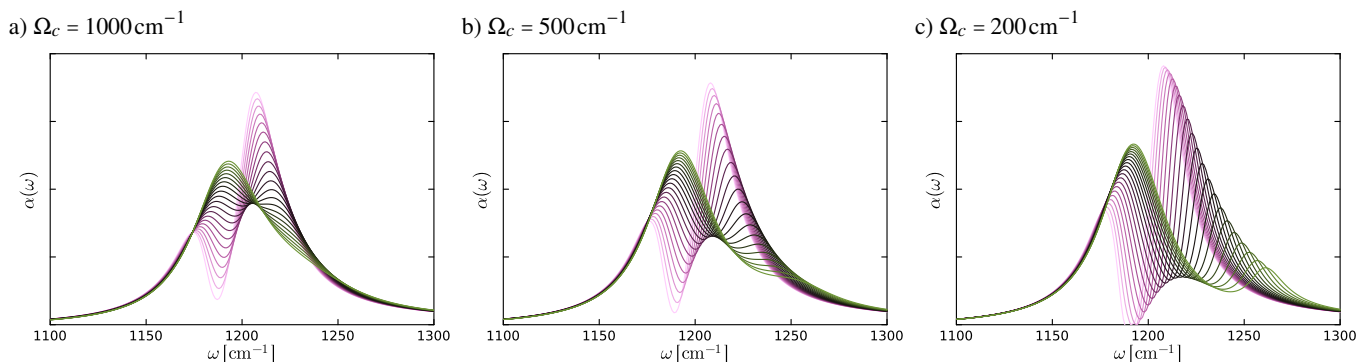


FIG. S4. Infrared absorption line shapes of a single molecule ($N_{\text{mol}} = 1$) inside the cavity for λ_c values ranging from 100 cm^{-1} (pink) to 300 cm^{-1} (green), with increments of 10 cm^{-1} . Each panel represents the spectra for a different cavity bath characteristic frequency Ω_c . The other simulation parameters are as follows: $\omega_c = 1185 \text{ cm}^{-1}$, $\eta_c = 0.00125 \text{ a.u.}$, $T = 300 \text{ K}$, and $d_c = 10$.

INFRARED ABSORPTION LINE SHAPES AND RATE MODIFICATION PROFILES IN THE SINGLE-MOLECULE LIMIT

Fig. S4 illustrates the absorption line shapes, $\alpha(\omega) \propto \frac{1}{2\pi} \int_{-\infty}^{\infty} dt e^{i\omega t} \langle \vec{\mu}(x,t) \vec{\mu}(x,0) \rangle$, which is obtained by performing the Fourier transform of the dipole-dipole auto-correlation function. These absorption spectra are calculated for cavity damping strengths λ_c ranging from 100 cm^{-1} to 300 cm^{-1} , covering the turnover observed in Fig.2 of the main text, and for three different values of the cavity bath's characteristic frequency Ω_c in the single-molecule limit.

The characteristic frequency of the cavity bath Ω_c is inversely related to the bath's characteristic timescale, with smaller Ω_c corresponding to slower bath response and more pronounced non-Markovian feature. In the Markovian limit ($\Omega_c = 1000 \text{ cm}^{-1}$), split double peaks corresponding to the upper and lower polaritons are observed for $\lambda_c < 250 \text{ cm}^{-1}$. These peaks broaden and blue shift as λ_c increases, although the Rabi splitting, i.e. the energy gap between two peaks, remains nearly constant, $\Omega_R = 32 \text{ cm}^{-1}$. In contrast, in the non-Markovian regime ($\Omega_c = 200 \text{ cm}^{-1}$), the Rabi splitting remains evident event at higher λ_c and increases from $\Omega_R = 32 \text{ cm}^{-1}$ for $\lambda_c = 100 \text{ cm}^{-1}$ to $\Omega_R = 68 \text{ cm}^{-1}$ for $\lambda_c = 300 \text{ cm}^{-1}$.

In addition, the rate modification profiles as a function of the cavity frequency ω_c are shown in Fig. S5 for various λ_c with a fixed characteristic frequency of the cavity bath, $\Omega_c = 1000 \text{ cm}^{-1}$. As λ_c increases, the resonant peak first shifts to larger ω_c before reversing direction. This shift arises from the broadening effects of the molecular vibrational and cavity photonic states due to their coupling with the baths. For the double-well model considered in this work, two vibrational transitions with the energies 1140 cm^{-1} and 1238 cm^{-1} are involved in the reaction mechanisms. Photons with frequencies between these two vibrational transitions can trigger either transition, enabling an additional cavity-induced intramolecular reaction pathway and then altering the reaction rate, as analyzed in our previous work.^{S1} The peak position also varies with changes in the molecule-solvent

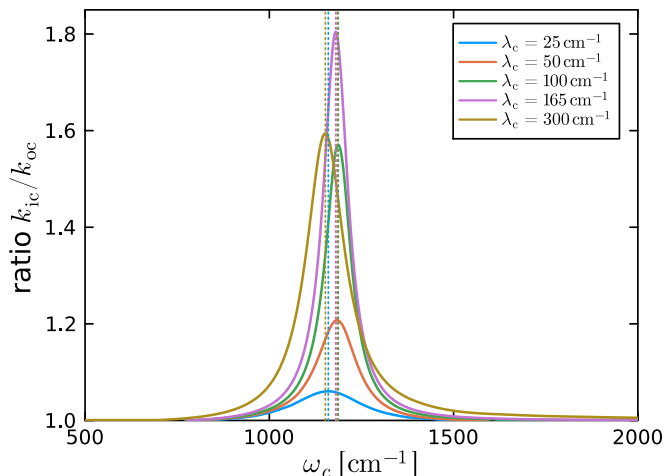


FIG. S5. Rate modification profile as a function of the cavity frequency in the single-molecule limit for different values of the cavity damping strength, λ_c . The vertical dotted lines in the figure mark the position of the peaks. Other parameters used in the simulations are $\Omega_c = 1000 \text{ cm}^{-1}$, $\eta_c = 0.00125 \text{ a.u.}$, $T = 300 \text{ K}$, and $d_c = 10$.

coupling strength (λ_i), the light-matter coupling strength η_c .^{S2} Furthermore, as the system approaches stochastic resonance, i.e. the optimal intermediate noise level at $\lambda_c = 165 \text{ cm}^{-1}$, the peak becomes sharper and stronger, before broadening and weakening with further increase in the cavity damping strength λ_c .

The peak positions and full width at half maximum (FWHM) values for different λ_c are summarized below:

$\lambda_c [\text{cm}^{-1}]$	25	50	100	165	300
Peak position [cm^{-1}]	1160	1184	1187	1180	1152
FWHM [cm^{-1}]	205	125	85	80	125

Interestingly, a sharp resonant peak in the rate modification profile can be observed regardless of whether the Rabi splitting is present (e.g. when $\lambda_c = 100 \text{ cm}^{-1}$) or absent (e.g. when $\lambda_c = 300 \text{ cm}^{-1}$). In the vibrational strong coupling regime, characterized by Rabi splitting significantly exceeding the FWHM of the split peaks in the absorption line shapes, e.g. when $\lambda_c < 50 \text{ cm}^{-1}$, only a broad and weak resonant peak is observed. These results suggest that observing a Rabi splitting is neither a necessary nor a sufficient condition for the emergence of pronounced resonant rate modification in vibrational polariton chemistry.

IMPORTANCE OF HIGHER PHOTONIC EXCITATION MANIFOLD

In the main text, it has been demonstrated that accounting for higher photonic excitation states is essential for accurately capturing reaction dynamics, particularly in the collective coupling regime. When only the lowest photonic excited state ($d_c = 2$) is considered, both the reaction rates and the damping of oscillations in the rescaled flux-side correlation function $k(t)$, and the average photonic excitation number $\langle n_c(t) \rangle$, are significantly underestimated. This is illustrated in Fig. S6 for the case of $N_{\text{mol}} = 4$.

Furthermore, even in the single-molecule limit, the inclusion of higher photonic excitation states is critical. Fig. S7 compares the results for the light-matter coupling strength $\eta_c = 0.005 \text{ a.u.}$ with $d_c = 2$ and $d_c = 10$, the latter representing the convergent solution. Neglecting multi-photon processes leads not only to incorrect predictions of the resonant peak in the rate modification profile as a function of the cavity frequency ω_c , but also to an overestimation of the turnover λ_c in the stochastic resonance effect.

These findings underscore the importance of considering the higher photonic excitation manifold to accurately capture the interplay between light-matter coupling and vibrational dynamics in both single-molecule and collective scenarios.

IMPACT OF VARIOUS NOISE LEVELS IN COLLECTIVE COUPLING REGIME

Fig. S8 displays the ratio of rates k_{i_c}/k_{o_c} as a function of N_{mol} for varying levels of noise (λ_c). In a lossless cavity ($\lambda_c = 0 \text{ cm}^{-1}$) and a weak cavity damping scenario ($\lambda_c = 50 \text{ cm}^{-1}$), reaction rates inside the cavity exhibit a rapid increase as the number of molecules aggregates. At an intermediate noise level ($\lambda_c = 100 \text{ cm}^{-1}$), the rate enhancement initially rises with

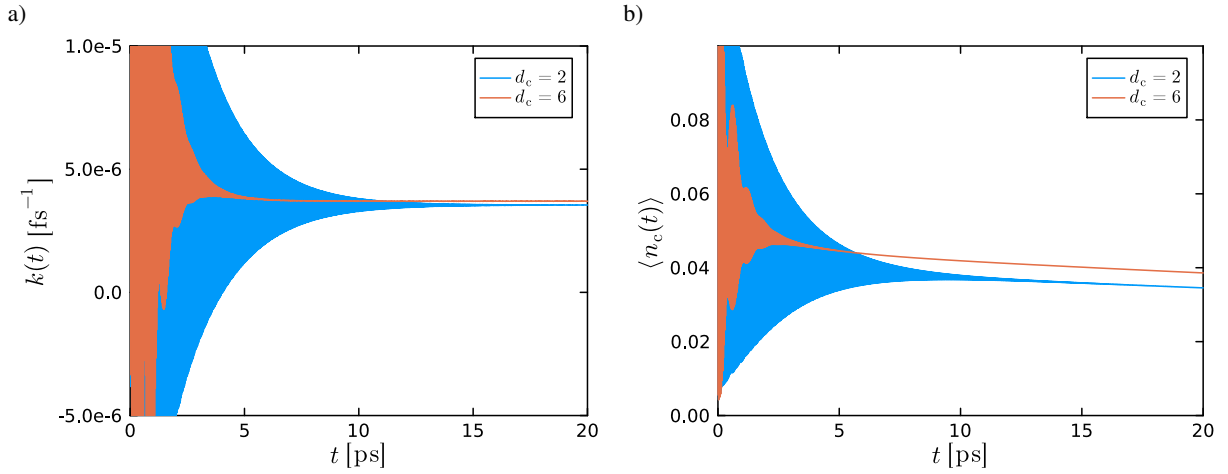


FIG. S6. Rescaled flux-side correlation function $k(t)$ (panel a) and the dynamics of the average photonic excitation number $\langle n_c(t) \rangle$ (panel b) for simulations including two ($d_c = 2$) and ten ($d_c = 10$) lowest photonic states. Other parameters used in the simulations are $\lambda_c = 50 \text{ cm}^{-1}$, $\Omega_c = 1000 \text{ cm}^{-1}$, $\omega_c = 1185 \text{ cm}^{-1}$, $\eta_c = 0.00125$ a.u., $T = 300 \text{ K}$, and $N_{\text{mol}} = 4$. These results underscore the necessity of including higher photonic states for accurate modeling in the collective coupling regime.

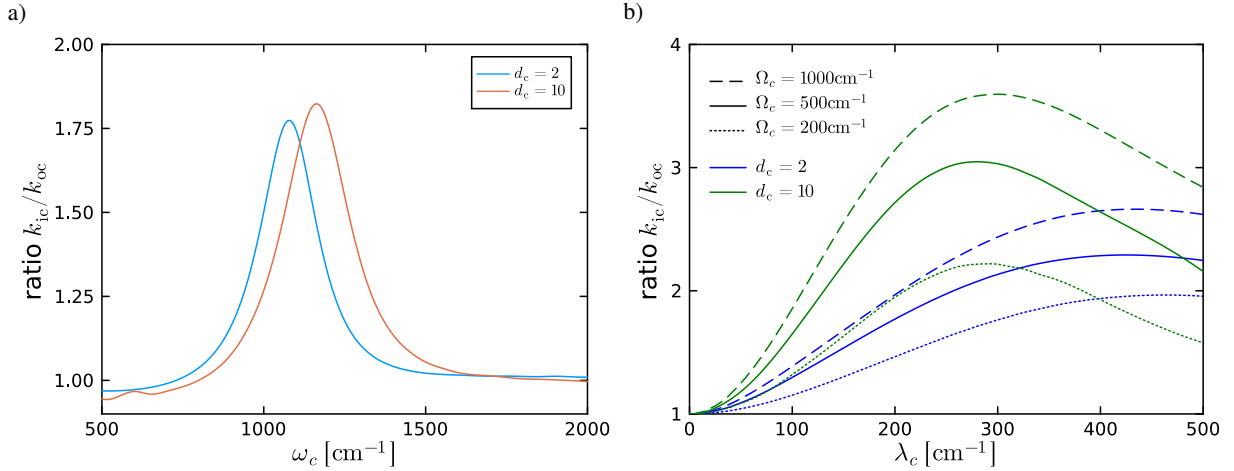


FIG. S7. a) Rate modification profile k_{ic}/k_{oc} as a function of the cavity frequency ω_c for single-molecule simulations including two ($d_c = 2$) and ten ($d_c = 10$) lowest photonic excited states, respectively. The parameters for the cavity bath are $\lambda_c = 100 \text{ cm}^{-1}$ and $\Omega_c = 1000 \text{ cm}^{-1}$. The light-matter coupling strength is $\eta_c = 0.005$ a.u., which results in a Rabi splitting of $\Omega_R = 108 \text{ cm}^{-1}$ under the resonant condition. b) Ratio of rate k_{ic}/k_{oc} as a function of λ_c for three different cavity bath characteristic frequencies Ω_c under resonant condition ($\omega_c = 1185 \text{ cm}^{-1}$), strong light-matter coupling ($\eta_c = 0.005$ a.u.), single-molecule ($N_{\text{mol}} = 1$) limit. The blue and green lines correspond to simulations with $d_c = 2$ and $d_c = 10$, respectively. The temperature is set at $T = 300 \text{ K}$. These results highlight the importance of multi-photon processes in accurate rate predictions in the strong light-matter coupling regime.

N_{mol} but then declines as the number of molecules continues to grow. For a stronger cavity damping ($\lambda_c = 165 \text{ cm}^{-1}$), the rate enhancement steadily diminishes with increasing N_{mol} . However, in the case of ultrastrong damping ($\lambda_c = 300 \text{ cm}^{-1}$), while the rate enhancement in the single-molecule limit is not substantial, it declines very slowly with the addition of more connected molecules.

These results highlight the strong dependence of stochastic resonance on system size, i.e. the number of molecules in a molecular network connected by the cavity mode. As seen in Fig. S8, the sensitivity of the rate modification to λ_c is reduced in larger systems, with a notable rate enhancement even in the weak cavity damping regime. This behavior is likely attributed to the rapid increase in the number of cavity-induced intermolecular reaction pathways,^{S1} which grows proportionally to $N_{\text{mol}} \times (N_{\text{mol}} - 1)/2$, binding all molecules together in the collective process. Further studies will delve deeper into the relationship of the reactivity and the degree of intermolecular delocalization in large systems.

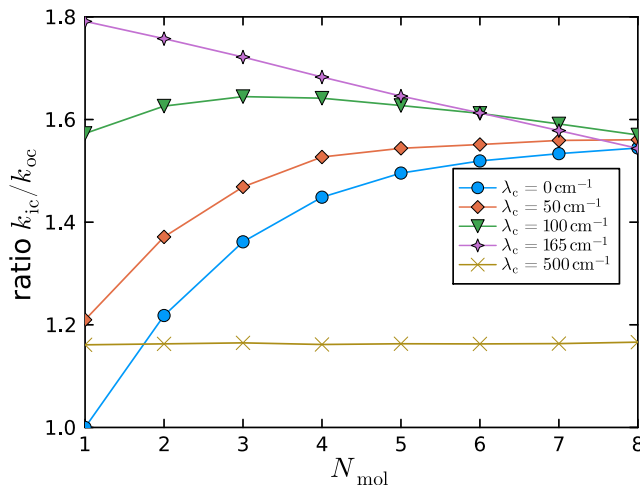


FIG. S8. Ratio of rates k_{ic}/k_{oc} as a function of the number of molecules collectively coupled to the cavity mode for varying values of λ_c . Other parameters used in the simulations are $\omega_c = 1185 \text{ cm}^{-1}$, $\Omega_c = 1000 \text{ cm}^{-1}$, $\eta_c = 0.00125 \text{ a.u.}$, $T = 300 \text{ K}$, and $d_c = 8$.

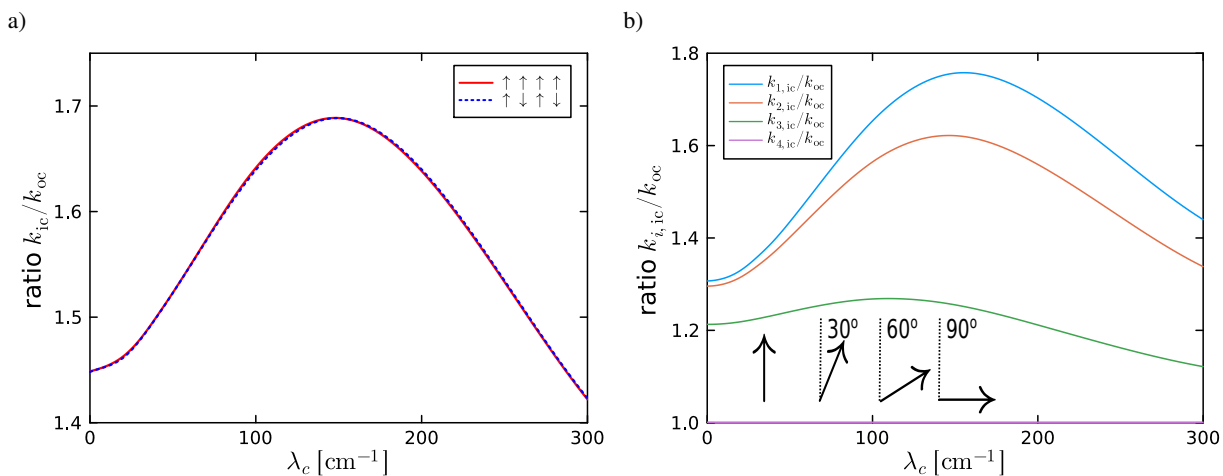


FIG. S9. a) Ratio of rates k_{ic}/k_{oc} as a function of the cavity damping strength λ_c for $N_{\text{mol}} = 4$. The red solid line represents the aligned dipole configuration, where all molecular dipoles are aligned with the light polarization ($\theta_i = 0$). The blue dotted line corresponds to the configuration where the molecular dipoles of the first and third molecules align with the light polarization ($\theta_{1/3} = 0$), while those of the second and fourth molecules point in the opposite direction ($\theta_{2/4} = \pi$). b) Ratio of rates $k_{i,ic}/k_{oc}$ for individual molecules as a function of λ_c in a misaligned molecular ensemble with $N_{\text{mol}} = 4$. The dipole angles relative to the light polarization are $\theta_i = (i-1)\pi/6$, leading to progressively weaker effective light-matter coupling strength for molecules further misaligned from the light polarization axis. The first molecule ($\theta_1 = 0$) achieves the maximum coupling strength, exhibiting larger rate enhancements and higher turnovers in λ_c , while the fourth molecule ($\theta_4 = \pi/2$) is fully decoupled from the cavity mode, showing no rate modification across the entire λ_c range. Other parameters used in the simulations are $\omega_c = 1185 \text{ cm}^{-1}$, $\Omega_c = 1000 \text{ cm}^{-1}$, $\eta_c = 0.00125 \text{ a.u.}$, $T = 300 \text{ K}$, and $d_c = 8$.

IMPACT OF DIPOLE ORIENTATIONS

In our prior study,^{S1} we have demonstrated that for a dimer, as long as the molecular dipoles are in line with the light polarization ($\cos \theta_i = \pm 1$ in $\vec{\mu}_i(x_i) \cdot \vec{e} = x_i \cos \theta_i$), the reaction rates remains unchanged regardless of whether $\theta_i = 0$ or $\theta_i = \pi$, although the transient dynamics are significantly influenced by the molecular dipole orientation. This phenomenon persists even with more molecules. Specifically, reaction rates are invariant to the sign in $\cos \theta_i$. An example with $N_{\text{mol}} = 4$ and two molecular dipole configurations is presented in Fig. S9a. This invariance can be explained by the dependence of cavity-induced intramolecular and intermolecular reaction pathways on $(\vec{\mu}_i(x_i) \cdot \vec{e})^2$, as detailed in Ref. S1.

Furthermore, cavity-induced intermolecular reaction pathways differ from cavity-induced intramolecular reaction pathways, in that they do not require cavity thermalization with the cavity bath. Consequently, in a lossless cavity ($\lambda_c = 0$), cavity-induced

rate modification arises solely from cavity-induced intermolecular reaction pathways, which require the overlap of vibrational transition energies in different molecules and the cavity frequency.

In a molecular ensemble, where each molecule has a distinct orientation, reaction rates vary between molecules. Fig. S9b illustrates the reaction rates as a function of λ_c for different molecules in a molecular ensemble with $N_{\text{mol}} = 4$. The first molecule is aligned along the light polarization, achieving the maximum light-matter coupling strength η_c . The second and third molecules are oriented at angles of $\pi/6$ and $\pi/3$ to the light polarization, resulting in effective light-matter coupling strength per molecule of $\sqrt{3}\eta_c/2$ and $\eta_c/2$, respectively. These reduced coupling strengths lead to lower reaction rates and smaller turnover values of λ_c . The fourth molecule, with its dipole moment perpendicular to the light polarization, is decoupled from the cavity and other molecules, showing no rate modification inside the cavity. Therefore, in a realistic molecular ensemble collectively coupled to the cavity mode, the disparity in reaction rates per molecule due to their distinct dipole orientations raises questions about how to define a group rate for such a system. This remains an open issue in rate theory and warrants further investigation.

[S1]Y. Ke and J. O. Richardson, "Insights into the mechanisms of optical cavity-modified ground-state chemical reactions," *J. Chem. Phys.* **160**, 224704 (2024).

[S2]Y. Ke and J. O. Richardson, "Quantum nature of reactivity modification in vibrational polariton chemistry," *J. Chem. Phys.* **161**, 054104 (2024).